JOURNAL OF GUIDANCE, CONTROL, AND DYNAMICS
Vol. 40, No. 9, September 2017

Nonlinear Kalman Filtering for Improved Angles-Only Navigation Using Relative Orbital Elements

Joshua Sullivan* and Simone D'Amico†
Space Rendezvous Laboratory, Stanford University, Stanford, California 94305-4035

DOI: 10.2514/1.G002719

This paper addresses the design and validation of an accurate estimation architecture for autonomous angles-only navigation in orbits of arbitrary eccentricity. The proposed filtering strategy overcomes the major deficiencies of existing approaches in the literature, which mainly focus on applications in near-circular orbits and generally suffer from poor dynamical observability due to linearizing the filter dynamics and measurement models. Consequently, traditional angles-only navigation solutions require conducting known orbital maneuvers to reconcile the ambiguous range. In contrast, the algorithms developed in this work enable accurate maneuver-free reconstruction of the relative orbital motion. This is done through the full exploitation of nonlinearities in the measurement model using the unscented Kalman filter to improve dynamical observability and filter performance. The filter estimates mean relative orbit elements, adopting a state transition matrix subject to secular and long-period J_2 perturbation effects to decouple observable from unobservable parameters. The complete state is then reconciled with the angle measurements in the measurement model through a nonlinear transformation that includes the conversion from mean to osculating orbital elements. The resulting linear dynamics model is supplemented by either first-order Gauss–Markov processes (that is, differential empirical accelerations) or by a covariance-matching approach to online adaptive process noise tuning to increase performance at minimal computational complexity. Finally, the estimation architecture is completed by a novel deterministic algorithm for batch initial relative orbit determination to accurately initialize the sequential filter.

I. Introduction

FUTURE space missions involving the interaction of multiple satellites present increasingly demanding relative navigation requirements that must be achieved autonomously using limited onboard resources. The research presented in this paper considers a particularly useful relative navigation scenario wherein an observing spacecraft is navigating with respect to a target space object at large separations (several kilometers) using only bearing angles obtained by a single onboard camera. This so-called angles-only navigation provides an inherently passive, robust, and high-dynamic range capability that uses simple sensors that are already on board most spacecraft. Furthermore, because of their low-cost, low power consumption, and small form factor as compared with other metrology systems like lidar and radar, these sensors enable accurate relative navigation while complementing the current trend of spacecraft miniaturization. Accordingly, angles-only navigation represents a clear enabling technology for a variety of advanced multi-satellite mission concepts [1]. These include robust autonomous rendezvous and docking [2,3], improved space situational awareness, advanced distributed aperture science (see, for example, the miniaturized distributed occulter/telescope project in development at Stanford University [4]), and on-orbit servicing of noncooperative spacecraft [5–7]. In line with the terminology of the last application, this paper denotes the observing spacecraft as "the servicer" and treats its orbit as the reference about which to describe the relative orbital motion of the target.

The angles-only navigation problem has been explored in several research studies, both from the perspective of developing and evaluating the analytical framework for relative state estimation using bearing angles and in the lens of designing and achieving in-flight demonstrations. In general, the majority of previous literature operates under the well-documented claim that the angles-only navigation problem is not fully observable due to a lack of explicit range information. The work of Woffinden and Geller [8] clarified this claim by providing closed-form sufficient conditions for observability using a linearized relative motion model in rectilinear coordinates. The conclusion was that, when formulating the angles-only navigation dynamical system, using purely linear models for the dynamics and measurements yielded an unobservable system whereby the complete relative motion state could not be reconstructed from sequences of bearing angles. Gaias et al. [9] explored the use of a relative orbital element (ROE)-based description for the relative motion, and they showed an improved physical interpretation wherein the unobservability problems were confined to a single state element that best approximated the ambiguous range. Furthermore, the inclusion of the J_2 perturbation was shown to improve the mathematical metrics for observability, namely, through the decrease of the condition number of the so-called observability matrix. Still, the most common method employed by researchers to mitigate the unobservability, and the one taken by Woffinden and Geller [10] and Gaias et al. [9], is to conduct designated orbital maneuvers that produce a known variation to the natural bearing angle trends. This approach has the undesirable effect of strongly coupling the achievable relative navigation accuracy with the maneuver-planning task, and it must be repeated periodically to correct filter estimate divergence. Instead, recent work by Sullivan et al. [11] formulated a novel procedure for angles-only navigation that does not require designated orbital maneuvering for successful relative motion estimation in near-circular low Earth orbit (LEO). The authors leveraged the same ROE state as discussed previously, and they instituted an estimation architecture that included nonlinear effects related to the mean-to-osculating transformation when mapping variations of the measured bearing angles to variations in the modeled J_2-perturbed relative motion. However, several limitations existed within that research, including inconsistent filter performance for several common relative motion configurations, slow convergence rates for the estimation of the ROE state, and sensitivity to the selected filter tuning parameters.

Presented as Paper 17-402 at the 27th AAS/AIAA Space Flight Mechanics Meeting, San Antonio, TX, 5–9 February 2017; received 31 January 2017; revision received 5 May 2017; accepted for publication 6 May 2017; published online 26 June 2017.

*Doctoral Candidate, Department of Aeronautics and Astronautics, Durand Building, 496 Lomita Mall.

†Assistant Professor, Director of the Space Rendezvous Laboratory, Department of Aeronautics and Astronautics, Durand Building, 496 Lomita Mall.

In the framework of the ARGON (advanced rendezvous demonstration using GPS and optical navigation) and AVANTI (autonomous vision approach-navigation and target identification) in-flight demonstrations, the research studies of D'Amico et al. [2] and Gaias et al. [3] provided compelling evidence showing that the unobservability decoupling and practical collision-avoidance constraints based on the E/I-vector separation principle [12] enabled successful reconstruction of the ROE state in near-circular orbits when applied in conjunction with orbital maneuvers. The ARGON mission was able to demonstrate angles-only rendezvous from tens of kilometers down to 2 km of separation in LEO using ground-in-the-loop image processing and relative orbit determination. Instead, the recently completed AVANTI mission achieved autonomous angles-only navigation and rendezvous from tens of kilometers to within 30 m of separation with a designated navigation filter using the ROE to estimate the J_2- and differential-drag-perturbed relative motion in LEO. These demonstrations provided useful insight into the constraints imposed by a real-world implementation of angles-only relative navigation.

As a final consideration, the problem of angles-only initial relative orbit determination (IROD) is of great utility to both general space situational awareness and to the completion of an encompassing angles-only sequential filtering framework. An accurate and computationally efficient IROD tool can provide the necessary initialization to begin sequential angles-only filtering. In this context, Sullivan et al. [11] developed an IROD tool that used a reduced set of ROE nondimensionalized by the relative mean longitude to estimate the shape and orientation of the relative motion in near-circular unperturbed orbits. That method neglected the dynamical evolution of the reduced ROE set and required substantial measurement time and prior knowledge on the relative separation to fully initialize the sequential estimation of the ROE state. Instead, Geller and Lovell [13] explored the use of a second-order expansion of the measurement model, combined with the linear Hill–Clohessy–Wiltshire (HCW) dynamics model in spherical coordinates, to provide an approximate IROD solution for unperturbed, circular orbits. The work of Newman et al. [14] investigated a two-part methodology that used a linear expansion of the measurement equations to solve for the initial state vector, which was then scaled using a nonlinear Volterra expansion of the dynamics in circular unperturbed orbits. Finally, the previously mentioned ARGON and AVANTI missions relied on prior orbital knowledge of the target provided by the North American Aerospace Defense Command's (NORAD's) two-line elements (TLEs) and designated radar campaigns, respectively, to fully initialize the estimation procedures without using bearing angle measurements at all.

This paper primarily addresses the limitations of the previous maneuver-free approach of Sullivan et al. [11] through the following main contributions to the state of the art. First, a novel deterministic method for angles-only IROD is developed for general application in J_2-perturbed orbits of arbitrary eccentricity. The approach leverages the ROE state in order to decouple the strongly observable relative orbit geometry from the ambiguous range, resulting in a system of linear equations that are analytically solved to obtain the initial ROE unit vector. To appropriately scale the initial unit vector solution, two options are explored. First, a second-order expansion of the measurement equations yields a system of quadratic equations that must be solved for the scaling factors. Instead, the second option uses coarse prior range knowledge that is supplemented by the known unit vector obtained from sparse imaging to arrive at the complete initialization. This latter method is shown to reduce the amount of bearing angle measurements required for high performance, minimize the reliance on prior target orbit knowledge, and provide accurate initial ROE estimates to the sequential filter without using orbital maneuvers. Then, an innovative design procedure is conducted with the objective of developing a completely maneuver-free sequential state estimation architecture that yields accurate and robust performance with minimal increase in complexity for eccentric orbit scenarios. The filtering approach developed in this paper is founded on nonlinear variants of the seminal Kalman filter (KF) methodology originally presented by Rudolf Kalman [15–17] in the context of estimation for linear systems. Notably, the extended KF (EKF) discussed by Bucy [18] and the unscented KF (UKF) presented by Julier and Uhlmann [19] are considered because they allow the powerful linear KF approach to be applied to systems with nonlinear dynamics and/or measurement models. In an effort to retain simplicity of the filtering frameworks, purely linear dynamics models that capture the secular J_2 perturbation effects on the mean ROE are implemented instead of complex numerical integration methods for nonlinear dynamics propagation. To overcome the tight observability constraints imposed by maneuver-free angles-only navigation, the filter measurement model retains an appropriate nonlinear mean-to-osculating orbital element transformation. In doing so, the separation-dependent osculating characteristics of the measured bearing angles are more effectively related back to variations in the estimated ROE state parameters. This keen insight into the perturbed dynamics, combined with a better capturing of the orbit curvature through the nonlinear mapping from orbital elements to position and velocity, is demonstrated to be the key to unlocking practical filter improvement. With these fundamental considerations handled, the scope of the design process transitions to improving filter accuracy and robustness. To that end, an inventive and simplistic framework is developed and implemented to estimate the camera sensor biases and empirical differential accelerations in addition to the ROE. These quantities directly supplement modeling deficiencies in the relative orbital dynamics with a limited increase in complexity. As an alternate design strategy, a novel adaptive angles-only filtering framework is presented whereby the process noise statistics are tuned online using sequences of measurement residuals to improve filter process modeling and proactively minimize sensitivity to filter noise statistics parameters that are instead often chosen through trial and error. The overall result is an estimation architecture that has been pragmatically improved to maximize the potential dynamical observability and filtering performance while still decoupling the navigation process from the maneuver-planning problem. Finally, the performance of the navigation algorithms is validated in high fidelity against rigorous numerically propagated force models, subject to realistic constraints on sensor performance. From a practical perspective, this accurate and robust maneuver-free angles-only methodology enables computational- and fuel-efficient estimation while still meeting the strict navigational requirements posed by multi-satellite mission concepts.

After this introduction, Sec. II highlights the overall dynamical system formulation that provides the foundation for estimating the relative motion as encoded by a set of relative orbital elements. The problem of filter initialization through initial relative orbit determination is addressed in Sec. III, and the design and validation of the maneuver-free navigation architecture are conducted in Sec. IV. Finally, Sec. V offers concluding remarks and lessons learned on the topic.

II. Development of the Dynamical System Representation

The angles-only navigation problem studied in this paper involves estimating the relative state of a target space object with respect to an observing servicer spacecraft in eccentric orbits using only bearing angle measurements from a camera sensor on board the servicer spacecraft. Scenarios are considered that emulate far- to midrange operations, with separations ranging from tens of kilometers to a few hundred meters. Although it is assumed that the initial relative state is unknown, there may be coarse prior information available to initialize the navigation procedure. The estimation problem is fully posed by the received measurements and by the choice of state to be reconstructed.

The available measurements are synchronous bearing angles, here denoted as the azimuth α and elevation ϵ, which subtend the rectilinear relative position vector pointing from the servicer spacecraft to the target space object: $\delta\boldsymbol{r}^{\mathcal{C}} = (\delta r_x^{\mathcal{C}}, \delta r_y^{\mathcal{C}}, \delta r_z^{\mathcal{C}})^{\mathrm{T}}$. The superscript $\mathcal{C}$ indicates that this line-of-sight (LOS) vector is described in the servicer camera frame, which has a known orientation with respect to the servicer reference frame. The servicer

reference frame is denoted as the radial/along-track/cross-track (RTN) frame and is compactly indicated with superscript $\mathcal{R}$. The RTN frame is centered on and rotates with the servicer spacecraft, and it is composed of orthogonal basis vectors $\hat{\boldsymbol{R}}$ directed along the servicer absolute position vector $\hat{\boldsymbol{N}}$ in the direction of the servicer orbital angular momentum vector, and $\hat{\boldsymbol{T}} = \hat{\boldsymbol{N}} \times \hat{\boldsymbol{R}}$, which completes the right-handed triad. Because far- to midrange space rendezvous scenarios often begin from large separations in the (anti)flight direction, this paper assumes a camera with a boresight $\hat{z}^{\mathcal{C}}$ aligned in the antivelocity direction, $\hat{y}^{\mathcal{C}}$ aligned with the angular momentum vector of the servicer orbit $\hat{\boldsymbol{N}}$, and $\hat{x}^{\mathcal{C}}$ completing the right-handed triad without loss of generality. Note that this orientation differs from the RTN frame only by a rotation about $\hat{\boldsymbol{N}}$ by the instantaneous servicer flight-path angle φ_{fpa}. Figure 1 depicts the relationship between the bearing angles and the LOS vector, as well as the relevant camera and RTN frames.

The nonlinear measurement model that expresses the bearing angles as functions of the relative camera frame position is given by

$$\boldsymbol{y} = \begin{pmatrix} \alpha \\ \epsilon \end{pmatrix} = \begin{pmatrix} \arcsin(\delta r_y^{\mathcal{C}} / \|\delta \boldsymbol{r}^{\mathcal{C}}\|) \\ \arctan(\delta r_x^{\mathcal{C}} / \delta r_z^{\mathcal{C}}) \end{pmatrix} = \boldsymbol{h}(\delta \boldsymbol{r}^{\mathcal{C}}, t) \tag{1}$$

With regard to choosing the state variables to be estimated, several alternative representations exist for describing the evolution of the relative orbital motion, including relative position and velocity components in the servicer RTN frame, combinations of servicer and target orbital elements, Euler parameters, epicyclic parameters, and spheroidal elements. Sullivan et al. [20] provided a detailed survey of the relative motion dynamics models built from several of these parameterizations. For this paper, a state representation consisting of mean quasi-nonsingular ROEs composed of the following combination of mean absolute orbital elements is adopted:

$$\delta \boldsymbol{x}_{\text{oe}} = \begin{pmatrix} \delta a \\ \delta \lambda \\ \delta e_x \\ \delta e_y \\ \delta i_x \\ \delta i_y \end{pmatrix} = \begin{pmatrix} \delta a \\ \delta \lambda \\ \delta e c_\varphi \\ \delta e s_\varphi \\ \delta i c_\vartheta \\ \delta i s_\vartheta \end{pmatrix} = \begin{pmatrix} (a_t - a_s)/a_s \\ (u_t - u_s) + c_{i_s}(\Omega_t - \Omega_s) \\ e_t c_{\omega_t} - e_s c_{\omega_s} \\ e_t s_{\omega_t} - e_s s_{\omega_s} \\ i_t - i_s \\ s_{i_s}(\Omega_t - \Omega_s) \end{pmatrix} \tag{2}$$

Here, $u = M + \omega$ is the mean argument of latitude, a, e, i, Ω, ω, and M are the classical Keplerian orbital elements, and c and s denote the cosine and sine of the argument in the subscript, respectively. In this parameterization, δa is the relative semimajor axis, $\delta\lambda$ is the relative mean longitude, $\delta \boldsymbol{e}$ is the relative eccentricity vector with magnitude δe and phase φ, and $\delta \boldsymbol{i}$ is the relative inclination vector with magnitude δi and phase ϑ. This state remains valid for circular reference orbits, but it is singular for reference orbits that are strictly equatorial. In addition to this quasi-nonsingular state, Koenig et al. [21] also considered a set of fully singular and fully nonsingular ROE, and they provided conversions between the three state

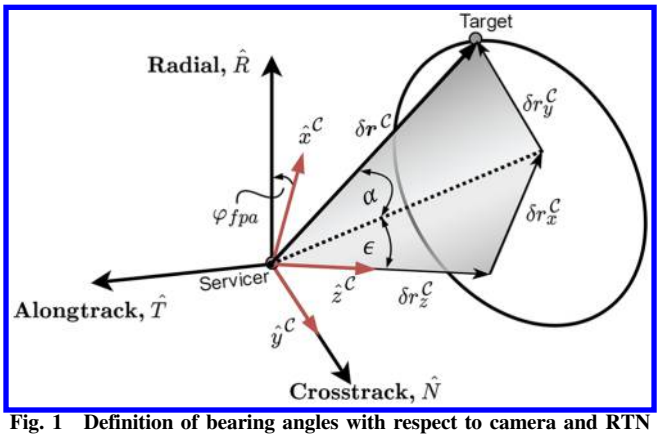

Fig. 1 Definition of bearing angles with respect to camera and RTN frame axes.

representations. In this paper, a distinction is made between mean elements, which describe the orbital motion subject to an averaged perturbation effect, and osculating elements, which instead describe the orbit that is instantaneously coincident with the true perturbed trajectory. Hereafter, $\tilde{(\cdot)}$ will explicitly indicate osculating elements or relative states composed of osculating elements (for example, $\tilde{a}$, $\delta\tilde{\boldsymbol{x}}_{\text{oe}}$, etc.) to distinguish from mean elements.

An application of averaging theory, in conjunction with the Gauss variational equations (GVE) and Lagrange planetary equations (LPE), provides an analytical framework for describing the secular and long-period effects caused by conservative and nonconservative perturbations on the ROE. Several authors have leveraged this advantage to solve the variational equations in closed form, providing relative motion dynamics models that are valid in the presence of higher-order geopotential, third-body gravity, atmospheric drag, and solar radiation pressure effects [21–23]. Furthermore, D'Amico and Montenbruck [12] and D'Amico [24] extensively formulated a powerful connection relating the mean ROE state of Eq. (2) to the relative motion geometry in near-circular orbits. The utility of that development was demonstrated in pragmatic guidance and control strategies that accounted for the slow ROE time variation under the influence of the J_2 Earth oblateness perturbation. Accordingly, the use of the same ROE in this paper is further motivated by a desire to extend these strategies and insightful geometric interpretations to the more general eccentric orbit cases.

In addition to reconstructing the ROE state, the angles-only scenario can be formulated to estimate other useful quantities. For this paper, the complete estimation state is given by

$$\boldsymbol{x}(t) = \begin{pmatrix} \delta \boldsymbol{x}_{\text{oe}} \\ \boldsymbol{b} \\ \delta \boldsymbol{a}_{\text{emp}}^{\mathcal{R}} \end{pmatrix} \in \mathbb{R}^{11} \tag{3}$$

where $\boldsymbol{b} = (b_\alpha, b_\epsilon)^{\text{T}} \in \mathbb{R}^2$ is the vector of azimuth and elevation sensor biases, and $\delta \boldsymbol{a}_{\text{emp}}^{\mathcal{R}} \in \mathbb{R}^3$ represents the vector of empirical differential accelerations expressed in the servicer RTN frame. The estimation of the ROE state is supplemented by the empirical accelerations to approximately capture unmodeled dynamics in the navigation algorithms, thus using a more computationally efficient method than numerically integrating the full differential equations of relative motion.

With the filter state chosen and the observables fixed, the foundation for the estimation problem is now formulated with an appropriate dynamical system representation. In the general angles-only relative navigation problem, both the dynamics describing the relative motion and the measurement model relating state elements to observations [see Eq. (1)] are nonlinear. Accordingly, the EKF and UKF architectures are employed because they include modifications to the linear KF algorithm to account for nonlinear systems. Although the UKF enables the nonlinear dynamics and measurement models to be used directly in the estimation (via the unscented transform), the EKF variant requires a first-order truncation of the dynamics and measurement model Taylor series expansions. Accordingly, this section develops the general dynamical system representation for the estimation problem and the linearized form necessary for the EKF architecture. In the latter case, the time evolution of the complete estimation state is governed by the system of differential equations:

$$\dot{\boldsymbol{x}}(t) = \boldsymbol{A}(t)\boldsymbol{x}(t) + \boldsymbol{B}(t)\boldsymbol{u}(t) + \boldsymbol{w}(t) \tag{4}$$

In the preceding equation, $\boldsymbol{A}(t) \in \mathbb{R}^{11\times 11}$ is the so-called plant matrix that captures the natural dynamics of the system, $\boldsymbol{B}(t) \in \mathbb{R}^{11\times 3}$ is the input sensitivity matrix relating RTN-frame control inputs, $\boldsymbol{u}(t) \in \mathbb{R}^3$, to the state evolution, and $\boldsymbol{w}(t) \in \mathbb{R}^{11}$ is zero-mean Gaussian white process noise [i.e., $\boldsymbol{w}(t) \sim \mathcal{N}(0_{11\times 1}, \boldsymbol{Q}(t))$ with covariance matrix $\boldsymbol{Q}(t) \in \mathbb{R}^{11\times 11}$]. Superposition of the zero input response and zero state response provides a complete solution to the preceding set of differential equations:

$$\boldsymbol{x}(t) = \boldsymbol{\Phi}(t, t_0)\boldsymbol{x}(t_0) + \int_{t_0}^{t} \boldsymbol{\Phi}(t, \tau)\boldsymbol{B}(\tau)\boldsymbol{u}(\tau)\,\mathrm{d}\tau \tag{5}$$

The state transition matrix (STM), $\boldsymbol{\Phi}(t, t_0) \in \mathbb{R}^{11\times 11}$, maps the state from time t_0 to time t, and it has the following structure composed of the individual STMs for each subset of the total estimation state:

$$\boldsymbol{\Phi}(t, t_0) = \begin{bmatrix} \boldsymbol{\Phi}_{\text{oe}} & 0_{6\times 2} & \boldsymbol{\Phi}_{\text{emp}}^{\text{oe}} \\ 0_{2\times 6} & \boldsymbol{\Phi}_b & 0_{2\times 3} \\ 0_{3\times 6} & 0_{3\times 2} & \boldsymbol{\Phi}_{\text{emp}} \end{bmatrix} \tag{6}$$

Each of the STMs in the preceding equation will be thoroughly detailed in the following sections. Note that, while $\boldsymbol{\Phi}_{\text{oe}}$, $\boldsymbol{\Phi}_b$, and $\boldsymbol{\Phi}_{\text{emp}}$ describe the direct propagation of their associated state subset from a previous time, $\boldsymbol{\Phi}_{\text{emp}}^{\text{oe}}$ captures the coupling effects of empirical accelerations on the dynamical evolution of the ROE. The filtering framework that leverages improved closed-form dynamics modeling to capture the most relevant perturbations in any Earth orbit regime. For this paper, the relative motion STM is used to incorporate only the dominant J_2 effects in eccentric orbit, which in general cause short-period (on the order of the orbital period) and long-period (on the order of the argument of perigee precession period) oscillations as well as secular drifts in the orbital elements. By substituting the first-order averaged J_2-perturbed potential into the LPE and effectively time averaging the ROE variational equations, the secular and long-period effects are captured in a linear time-varying dynamics model. As previously stated, Koenig et al. [21] formalized a modular procedure to build the STM for the time-varying system through a coordinate transformation to an intermediary time-invariant system. Due to the inherent decoupling of dynamics when using ROEs, the linearization does not truncate any terms with respect to $\delta\lambda$ and δi_y. Accordingly, the model is valid and highly applicable for scenarios involving large mean separations. The resulting STM for propagating the ROE over the interval $[t, t + \Delta t]$ is given by

$$\boldsymbol{\Phi}_{\text{oe}} = \begin{bmatrix} 1 & 0 & 0 & 0 & 0 & 0 \\ -\left(\frac{7}{2}\kappa EP - \frac{3}{2}n\right)\Delta t & 1 & \kappa e_{x0} FGP\Delta t & \kappa e_{y0} FGP\Delta t & -\kappa FS\Delta t & 0 \\ \frac{7}{2}\kappa e_{yf} Q\Delta t & 0 & c_{\dot{\omega}\Delta t} - 4\kappa e_{x0} e_{yf} GQ\Delta t & -s_{\dot{\omega}\Delta t} - 4\kappa e_{y0} e_{yf} GQ\Delta t & 5\kappa e_{yf} S\Delta t & 0 \\ -\frac{7}{2}\kappa e_{xf} Q\Delta t & 0 & s_{\dot{\omega}\Delta t} + 4\kappa e_{x0} e_{xf} GQ\Delta t & c_{\dot{\omega}\Delta t} + 4\kappa e_{y0} e_{xf} GQ\Delta t & -5\kappa e_{xf} S\Delta t & 0 \\ 0 & 0 & 0 & 0 & 1 & 0 \\ \frac{7}{2}\kappa S\Delta t & 0 & -4\kappa e_{x0} GS\Delta t & -4\kappa e_{y0} GS\Delta t & 2\kappa T\Delta t & 1 \end{bmatrix} \tag{9}$$

dynamics model linearization [Eq. (6)] is only strictly required by the EKF for updating the state covariance, whereas the UKF can use the full nonlinear dynamics to propagate the estimated state mean and covariance from a set of sigma points (i.e., estimate samples).

By expanding the nonlinear measurement model of Eq. (1) in a first-order Taylor series about the reference state, a linear measurement model can be formulated that takes the form

$$\boldsymbol{y}(t) = \boldsymbol{C}(t)\boldsymbol{x}(t) + \boldsymbol{\nu}(t) \tag{7}$$

Here, $\boldsymbol{y}(t) \in \mathbb{R}^2$ is the vector of modeled azimuth and elevation angles, $\boldsymbol{C}(t) \in \mathbb{R}^{2\times 11}$ is the measurement sensitivity matrix that relates variations in the propagated state $\boldsymbol{x}(t)$ to the modeled measurements, and $\boldsymbol{\nu}(t) \in \mathbb{R}^2$ is zero-mean Gaussian white measurement noise [i.e., $\boldsymbol{\nu}(t) \sim \mathcal{N}(0_{2\times 1}, \boldsymbol{R}(t))$ with covariance matrix $\boldsymbol{R}(t) \in \mathbb{R}^{2\times 2}$]. The measurement model linearization [Eq. (7)] is only strictly required for the EKF measurement update step.

Just as with the complete STM, the input sensitivity matrix $\boldsymbol{B}(t)$ and the measurement sensitivity matrix $\boldsymbol{C}(t)$ can be decomposed into forms with components corresponding to subsets of the complete estimation state:

$$\begin{aligned} \boldsymbol{B}(t) &= [\,\boldsymbol{B}_{\text{oe}} \quad \boldsymbol{B}_b \quad \boldsymbol{B}_{\text{emp}}\,]^{\text{T}} \\ \boldsymbol{C}(t) &= [\,\boldsymbol{C}_{\text{oe}} \quad \boldsymbol{C}_b \quad \boldsymbol{C}_{\text{emp}}\,] \end{aligned} \tag{8}$$

A. Relative Orbital Element Subset

The necessary system matrices for the relative motion state subset will now be developed in detail under the assumption of linear relative motion with respect to a servicer in an arbitrarily eccentric orbit. Relative motion perturbations due to J_2 and atmospheric drag are readily captured for eccentric orbits in the STMs developed by Koenig et al. [21]. Under the same mathematical framework as Koenig et al., Guffanti et al. [23] instead formulated a set of STMs that accounted for solar radiation pressure as well as sun and moon third-body gravity. From these works, it is possible to design a

where

$$\begin{aligned} &\gamma = \tfrac{3}{4}J_2 R_e^2\sqrt{\mu} \quad \eta = \sqrt{1 - \|\boldsymbol{e}\|^2} \quad \kappa = \gamma/a^{7/2}\eta^4 \quad G = \tfrac{1}{\eta^2} \\ &E = 1 + \eta \quad F = 4 + 3\eta \quad T = s_i^2 \quad \Delta t = t - t_0 \\ &P = 3c_i^2 - 1 \quad Q = 5c_i^2 - 1 \quad S = s_{2i} \quad \dot{\omega} = kQ \end{aligned} \tag{10}$$

The Earth's equatorial radius and gravitational parameter are denoted as R_e and μ, respectively, n is the servicer mean motion, and $\boldsymbol{e} = (e_x, e_y)^{\text{T}} = e_s(c_{\omega_s}, s_{\omega_s})^{\text{T}}$ denotes the servicer eccentricity vector. From now on, the absolute orbital elements that appear will always belong to the servicer spacecraft, so the subscript s will be dropped for ease of notation.

The structure of this STM provides insight into the evolution of the ROE due to J_2, which is useful for reconciling potential observability issues that arise due to only using bearing angle measurements. First, both $\delta\lambda$ and δi_y display constant drift, with the former resulting from combined Keplerian orbital motion and J_2 and the latter from only J_2. Additionally, the evolution of the relative eccentricity vector is marked by a secular drift perpendicular to the servicer eccentricity vector and a circular precession. An illustration of these trends is provided in Fig. 2. Although the established dynamics model only captures these secular and long-period variations in the mean ROE, it will be later shown how to incorporate the short-period oscillations in the measurement model of the EKF and UKF.

The measurement sensitivity matrix relating ROE variations to bearing angle variations, $\boldsymbol{C}_{\text{oe}}$, is developed using the following series of partial derivatives. Again, note that this linearized representation is required for the EKF formulation, whereas the UKF allows for the complete nonlinear measurement model to be retained in the recursion:

$$\boldsymbol{C}_{\text{oe}}(\delta\boldsymbol{x}_{\text{oe}}(t)) = \left.\frac{\partial \boldsymbol{y}}{\partial \delta\boldsymbol{x}_{\text{oe}}}\right|_{\delta\boldsymbol{x}_{\text{oe}}^{\text{ref}}} = \frac{\partial \boldsymbol{y}}{\partial \delta\boldsymbol{r}^{\mathcal{C}}} \cdot \frac{\partial \delta\boldsymbol{r}^{\mathcal{C}}}{\partial \delta\boldsymbol{r}^{\mathcal{R}}} \cdot \left.\frac{\partial \delta\boldsymbol{r}^{\mathcal{R}}}{\partial \delta\boldsymbol{x}_{\text{oe}}}\right|_{\delta\boldsymbol{x}_{\text{oe}}^{\text{ref}}} \tag{11}$$

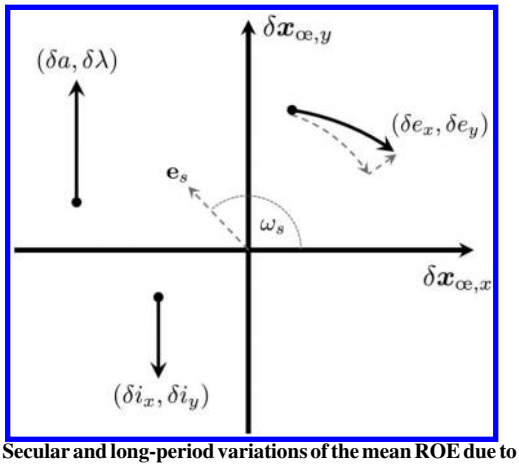

Fig. 2 Secular and long-period variations of the mean ROE due to the J_2 perturbation [21].

The rightmost term represents a linear mapping from ROE to the relative position in the servicer RTN frame. As previously stated, D'Amico [24] developed this mapping under the assumption of near-circular orbits by proving a first-order equivalence between the ROE of Eq. (2) and the integration constants of the rectilinear and curvilinear HCW model. That formulation leads to improved geometric insight whereby components of the ROE state correspond to features of the relative orbit trajectory. An analogous mapping with similar geometric benefit for the case of an arbitrarily eccentric reference orbit is not readily available, and will therefore be developed here.

The direct first-order mapping between nondimensional RTN-frame relative position components and Keplerian orbital element differences (OEDs) was provided by Casotto [25] and Schaub [26] as

$$\begin{aligned}
\frac{\delta r_R^{\mathcal{R}}(f)}{r(f)} &\approx \frac{\Delta a}{a} + \frac{e(1+ec_f)s_f}{\eta^3}\Delta M - \frac{(1+ec_f)c_f}{\eta^2}\Delta e \\
\frac{\delta r_T^{\mathcal{R}}(f)}{r(f)} &\approx \frac{(1+ec_f)^2}{\eta^3}\Delta M + \frac{(2+ec_f)s_f}{\eta^2}\Delta e + c_i\Delta\Omega + \Delta\omega \\
\frac{\delta r_N^{\mathcal{R}}(f)}{r(f)} &\approx s_\theta \Delta i - c_\theta s_i \Delta\Omega
\end{aligned} \tag{12}$$

where f and $\theta = f + \omega$ are the servicer true anomaly and true argument of latitude, $r(f)$ is the servicer orbital radius, and $\Delta(\cdot) = (\cdot)_t - (\cdot)_s$ implies an arithmetic difference of orbital elements.

It is straightforward to rewrite the ROE definitions of Eq. (2) in terms of OEDs and substitute into the preceding expressions. However, this does not immediately lead to a form of mapping that is geometrically insightful. Instead, a change of variables is introduced to include a modified relative mean longitude $\delta\lambda^*$ and a modified relative eccentricity vector $\delta\boldsymbol{e}^*$ with magnitude δe^* and phase φ^* given by

$$\begin{aligned}
\delta\lambda^* &= \xi\delta\lambda + (1-\xi)\left(-\frac{s_\omega}{e}\delta e_x + \frac{c_\omega}{e}\delta e_y + \cot i \delta i_y\right) \\
\delta e_x^* &= \frac{c_\omega \delta e_x + s_\omega \delta e_y}{\eta^2} = \delta e^* c_{\varphi^*} \\
\delta e_y^* &= \frac{-e\delta\lambda + e\cot i \delta i_y - s_\omega \delta e_x + c_\omega \delta e_y}{\eta^3} = \delta e^* s_{\varphi^*}
\end{aligned} \tag{13}$$

The auxiliary eccentricity factor ξ is defined as

$$\xi = \frac{1 + (1/2)e^2}{\eta^3} \tag{14}$$

By implementing this change of variables, Eq. (12) simplifies to

$$\begin{aligned}
\frac{\delta r_R^{\mathcal{R}}(f)}{r(f)} &\approx \delta a - \frac{e}{2}\delta e_x^* - \delta e^*\left(c_{\theta-\omega-\varphi^*} + \frac{e}{2}c_{2\theta-2\omega-\varphi^*}\right) \\
\frac{\delta r_T^{\mathcal{R}}(f)}{r(f)} &\approx \delta\lambda^* + \delta e^*\left(2s_{\theta-\omega-\varphi^*} + \frac{e}{2}s_{2\theta-2\omega-\varphi^*}\right) \\
\frac{\delta r_N^{\mathcal{R}}(f)}{r(f)} &\approx \delta i s_{\theta-\vartheta}
\end{aligned} \tag{15}$$

The mappings are now expressed in terms of the eccentric ROE (EROE) set: $\delta\boldsymbol{x}_{\text{oe}}^* = (\delta a, \delta\lambda^*, \delta\boldsymbol{e}^*, \delta\boldsymbol{i})^{\text{T}}$.

Recall from the relationships developed by D'Amico [24] that, in near-circular orbits, the radial and along-track relative motion are characterized by mean offsets given by δa and $\delta\lambda$, respectively, and oscillatory motion scaled by the magnitude of $\delta\boldsymbol{e}$. The cross-track motion displays oscillations scaled by the magnitude of $\delta\boldsymbol{i}$ and no mean offsets. Upon inspection of Eq. (15), an analogous interpretation for eccentric orbits is available. The radial motion still contains an offset due to δa and orbital-period periodic oscillations with amplitude scaled by $\delta\boldsymbol{e}^*$, but also an additional offset term due to a nonzero projection of the servicer eccentricity vector onto the relative eccentricity vector (i.e., $\delta e_x^* \neq 0$) and higher-order oscillatory motions with periodicity of twice the orbital period. The along-track motion is characterized now by an offset of $\delta\lambda^*$, and first- and second-order oscillations of amplitude proportional to $\delta\boldsymbol{e}^*$. The first-order oscillations in the along-track/radial plane trace out the well-known 2×1 ellipse seen in the circular case, and the second-order oscillations describe a circle of magnitude $e\delta e^*/2$. The cross-track motion maintains the same trends as in the circular case. Projection of the first-order oscillations in the cross-track/radial plane show the same general tilted ellipse with orientation given as a function of $\vartheta - \varphi^*$.

It is important to note that, under the assumptions of linearized Keplerian orbital motion, a difference in the semimajor axis results in a linear drift of $\delta\lambda$. Accordingly, $\delta\lambda^*$ and δe_y^* drift as well, resulting in radial and along-track oscillation magnitudes that are now time varying. The terms $\delta\lambda^*$ and δe_y^* are given as functions of their initial conditions and Keplerian variation over the propagation time Δt by

$$\delta\lambda^* = \delta\lambda_0^* + \frac{\partial\delta\lambda^*}{\partial\delta\lambda}\frac{\partial\delta\lambda}{\partial t}\Delta t \approx \delta\lambda_0^* - \frac{3}{2}\xi n \Delta t \delta a \tag{16}$$

$$\delta e_y^* = \delta e_{y0}^* + \frac{\partial\delta e_y^*}{\partial\delta\lambda}\frac{\partial\delta\lambda}{\partial t}\Delta t \approx \delta e_{y0}^* + \frac{3e}{2\eta^3} n \Delta t \delta a \tag{17}$$

Expanding the relative eccentricity vector terms in Eq. (15) and substituting in Eqs. (16) and (17) yields

$$\frac{\delta\boldsymbol{r}^{\mathcal{R}}(f)}{r(f)} \approx \boldsymbol{\phi}\delta\boldsymbol{x}_{\text{oe}}^* \tag{18}$$

where

$$\boldsymbol{\phi} = \begin{bmatrix}
1 & -\frac{3e}{2\eta^3}ks_f n\Delta t & 0 & -kc_f & -ks_f & 0 & 0 \\
-\frac{3}{2\eta^3}k^2 n\Delta t & 1 & (k+1)s_f & -(k+1)c_f + (e/2) & 0 & 0 \\
0 & 0 & 0 & 0 & s_\theta & -c_\theta
\end{bmatrix} \tag{19}$$

with $k = 1 + ec_f$.

The matrix in Eq. (19) is the same used by Alfriend et al. ([27] p. 109) to compactly propagate the linearized solution developed by Yamanaka and Ankersen (YA) [28] for the relative position from a set of integration constants. Thus, it can be concluded that the integration constants of the YA solution share a first-order equivalence with the EROE set $\delta\boldsymbol{x}_{\text{oe}}^*(t_0)$. The equivalent velocity-related elements of the aforementioned matrix can be formulated in a similar manner by

substituting Eqs. (16) and (17) into Eq. (15) and differentiating with respect to f. Note that evaluating Eq. (19) at $\Delta t = 0$ provides the mapping from an instantaneous EROE (instead of initial EROE) to a relative position in the RTN frame.

Returning to the necessity of computing the rightmost partial derivative in Eq. (11), the term can be reformatted to use the relationships derived previously by writing

$$\left.\frac{\partial \delta \boldsymbol{r}^{\mathcal{R}}}{\partial \delta \boldsymbol{x}_{\text{oe}}}\right|_{\delta x_{\text{oe}}^{\text{ref}}} = \left.\frac{\partial \delta \boldsymbol{r}^{\mathcal{R}}}{\partial \delta \boldsymbol{x}_{\text{oe}}}\right|_{0} = \frac{\partial \delta \boldsymbol{r}^{\mathcal{R}}}{\partial \delta \boldsymbol{x}_{\text{oe}}^{*}} \frac{\partial \delta \boldsymbol{x}_{\text{oe}}^{*}}{\partial \delta \boldsymbol{x}_{\text{oe}}} \tag{20}$$

with the left partial written from Eq. (19) as

$$\frac{\partial \delta \boldsymbol{r}^{\mathcal{R}}}{\partial \delta \boldsymbol{x}_{\text{oe}}^{*}} = r(f)\boldsymbol{\phi}\Big|_{\Delta t=0} \tag{21}$$

and the right partial written from the relationship between ROE and EROE in Eq. (13).

The center term of $\boldsymbol{C}_{\text{oe}}$ in Eq. (11) corresponds to the attitude of the camera frame with respect to the servicer RTN frame, which is assumed to be known to the accuracy of commercially available attitude determination systems. Recalling the geometry of Fig. 1, the nominal camera frame attitude with respect to the RTN frame is represented as the combined rotation matrix

$$\frac{\partial \delta \boldsymbol{r}^{\mathcal{C}}}{\partial \delta \boldsymbol{r}^{\mathcal{R}}} = \boldsymbol{R}_{\mathcal{R}}^{\mathcal{C}} = \begin{bmatrix} 1 & 0 & 0 \\ 0 & 0 & 1 \\ 0 & -1 & 0 \end{bmatrix} \begin{bmatrix} c_{\varphi_{\text{fpa}}} & s_{\varphi_{\text{fpa}}} & 0 \\ -s_{\varphi_{\text{fpa}}} & c_{\varphi_{\text{fpa}}} & 0 \\ 0 & 0 & 1 \end{bmatrix} \tag{22}$$

where the right matrix imposes a rotation by the flight-path angle φ_{fpa} from the RTN frame to the frame containing the velocity vector direction, and the left matrix describes the permutation of the camera axes with respect to that latter frame.

Finally, the leftmost term of Eq. (11) is the sensitivity of the modeled measurements with respect to variations in the camera frame relative position vector. Gaias et al. [9] gave the expression in terms of modeled bearing angles as

$$\frac{\partial \boldsymbol{y}}{\partial \delta \boldsymbol{r}^{\mathcal{C}}} = \frac{1}{\|\delta \boldsymbol{r}^{\mathcal{C}}\|} \begin{bmatrix} -\sin\alpha\sin\epsilon & \cos\alpha & -\sin\alpha\cos\epsilon \\ \sec\alpha\cos\epsilon & 0 & -\sec\alpha\sin\epsilon \end{bmatrix} \tag{23}$$

To compute the modeled bearing angles needed in Eq. (23), it is necessary to map the propagated ROE state to a relative position in the servicer RTN frame and apply Eq. (22) followed by Eq. (1). Multiple linear and nonlinear mappings were considered by Sullivan et al. [11] in the context of an observability assessment and angles-only navigation filter validation in near-circular orbits. The approach taken in this paper leverages the insight gained from that research to formulate the necessary mapping in an effort to maximize estimation accuracy and potential filter observability. Accordingly, a nonlinear mapping is chosen whereby the estimated mean ROE and the known mean absolute orbital elements of the servicer are used to calculate the mean absolute orbital elements of the target [see Eq. (2)]. These mean absolute orbital element sets can then be converted to corresponding osculating sets through the mean-to-osculating transformation offered by Schaub and Junkins ([29] appendix F) and then used to compute the absolute position and velocity of the servicer and target. Finally, the relative position is calculated and mapped to the servicer RTN frame. This complete mapping takes a functional form $\boldsymbol{g}: \mathbb{R}^6 \mapsto \mathbb{R}^3$ given by

$$\delta r_j^{\mathcal{R}} = g_j(\delta \boldsymbol{x}_{\text{oe}}(t), \text{oe}_s(t)) \tag{24}$$

where $\text{oe}_s(t)$ is the servicer absolute orbital element state at time t, and $j \in \{R, T, N\}$ indexes the components of the RTN position vector. It is important to remember that the nonlinear measurement model instituted by the UKF uses this chain of transformations directly for each sigma point instead of computing Eq. (11) at each step.

Recall that the chosen dynamics model includes only the secular and long-period variations of the mean ROE due to J_2 and neglects the short-period oscillations characterizing the true osculating perturbed relative motion. In general, conservative perturbations cause short-period oscillations of the ROE with amplitudes proportional to $\delta\lambda$ (the mean separation). With regard to the J_2 perturbation, this is because short-period effects are a function of the mean argument of latitude of the individual satellite orbits. Instead, nonconservative perturbations cause short-period oscillations of the ROE with the amplitude proportional to the differential ballistic coefficient (spacecraft size and orientation). The short-period trends for conservative perturbations are particularly obvious in Fig. 3, where a numerical simulation of a J_2-perturbed relative motion trajectory has been conducted for illustration purposes. Note that, while qualitatively the same trends occur for eccentric reference orbits, the results of Fig. 3 are generated using a near-circular reference orbit ($a = 7200$ km and $e = 0.01$) for improved visualization.

Over the simulation, the mean separation is decreased from 20 km to nearly 0 km to demonstrate the separation-dependent variation in the osculating ROE evolution. As evidenced in Fig. 3, the amplitudes of the ROE short-period oscillations demonstrate a corresponding decrease as the separation declines. Because the bearing angle measurements are inherently osculating, it stands to reason that these short-period characteristics necessarily encode information about the separation that can be leveraged in the filter measurement modeling. In addition to the immediate benefit of accounting for periodic separation-dependent features in the relative motion, the inclusion of the nonlinear mean-to-osculating transformation also preserves the improved orbit curvature modeling coming from the ROE. By

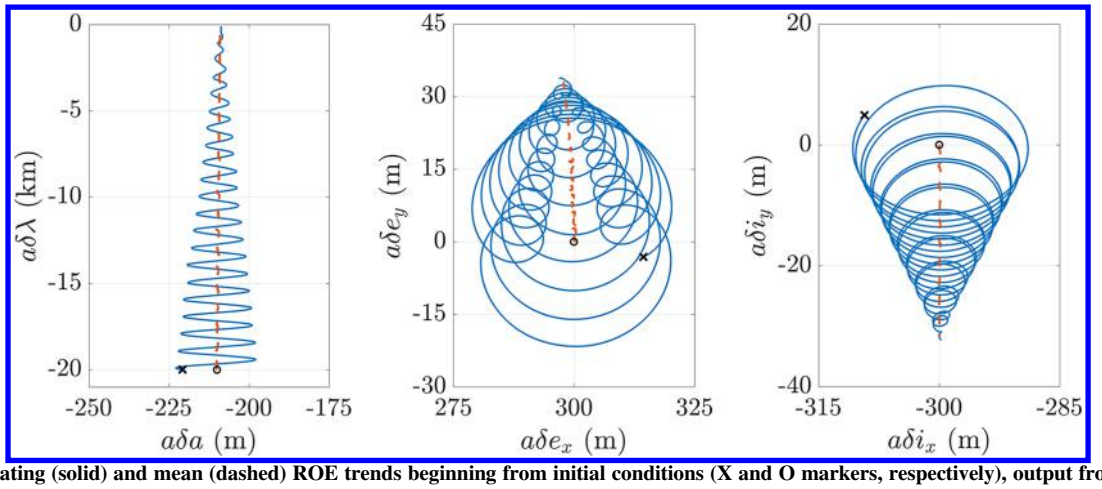

Fig. 3 Osculating (solid) and mean (dashed) ROE trends beginning from initial conditions (X and O markers, respectively), output from numerical propagation of J_2-perturbed equations of motion. Mean separation varies from 20 to 0 km. Simulated reference orbit is near-circular with a semimajor axis of 7200 km and eccentricity of 0.01.

definition, linearizing the transformation with respect to separation necessarily incurs a mismodeling of the orbit curvature. Accordingly, when combining a linear mean-to-osculating transformation with the nonlinear mapping from osculating orbital elements to position and velocity (which retains the improved curvature modeling), there is a mismatch between the observed and modeled bearing angles that precludes effective disambiguation of the separation. Instead, that mismatch is minimized by instituting the nonlinear mean-to-osculating transformation to also retain the orbit curvature effects. The result is a filter measurement model that better relates observed variations in the bearing angles to variations in the full ROE state. As an interesting illustration, one might attempt to confront the observability problem of angles-only estimation using the Gim–Alfriend dynamics model [30,31], which captures the evolution of the mean OED subject to secular J_2 perturbation effects in arbitrarily eccentric orbits, and subsequently applies a linear mapping to osculating OED followed by a linear mapping to the relative position and velocity elements. However, because the aforementioned mappings are linearized with respect to separation (as well as J_2 in the mean-to-osculating transformation), the same range-reconciling benefits as the approach suggested in this paper are not obtained. As a final example, consider that the state-of-the-art YA dynamics model for propagating the relative translational state in eccentric orbits [28] entirely neglects perturbations and the curvature of the orbit, thus precluding any functional observability improvements obtained by characterizing the perturbed dynamical environment of the angles-only navigation scenario.

In the event of servicer orbital maneuvering, the input sensitivity matrix, $\boldsymbol{B}_{\alpha}$, provides the link between an impulsive maneuver set in the servicer RTN principle directions, $\boldsymbol{u} = (\Delta v_R, \Delta v_T, \Delta v_N)^{\mathrm{T}}$, and the variation of the ROE. As in the near-circular case, where a first-order equivalence between the HCW integration constants and the ROE enables the input sensitivity matrix to be written from the inversion of the HCW solution [24,32], it is now possible to express $\boldsymbol{B}_{\alpha}$ from the inversion of the YA solution written in terms of the ROE through the previously established first-order correspondence between the EROE and YA integration constants. An equivalent formulation can also be derived from the GVE presented by Schaub and Junkins ([29] Chap. 14), which describe how the orbital elements evolve due to RTN-frame accelerations. Riggi and D'Amico [33] as well as Chernick and D'Amico [34] proceeded in this manner, and they presented a form of the variational equations relating impulsive maneuvers in the reference RTN frame to variations in the ROE state. The input sensitivity matrix from either of these methods is

$$\boldsymbol{B}_{\alpha} = -\frac{\eta}{an}\begin{bmatrix} \frac{2}{\eta^2}es_{f_m} & \frac{2k}{\eta^2} & 0 \\ \frac{(\eta-1)kc_{f_m}-2\eta e}{ek} & -\frac{(\eta-1)(k+1)s_{f_m}}{ek} & 0 \\ s_{\theta_m} & \frac{(k+1)c_{\theta_m}+e_x}{k} & \frac{e_y s_{\theta_m}}{k\tan i} \\ -c_{\theta_m} & \frac{(k+1)s_{\theta_m}+e_y}{k} & -\frac{e_x s_{\theta_m}}{k\tan i} \\ 0 & 0 & \frac{c_{\theta_m}}{k} \\ 0 & 0 & \frac{s_{\theta_m}}{k} \end{bmatrix} \tag{25}$$

where f_m and θ_m are the servicer true anomaly and true argument of latitude, respectively, at the maneuver instance. It is worth noting that certain modifications to the ROE can be made to decouple the preceding input sensitivity matrix. In [33], a modified $\delta\lambda$ is introduced to remove the effect of a tangential impulse on that element; in [34], a modified set of relative eccentricity vector parameters is shown to remove the cross-track impulse coupling with those elements. To maintain a consistent state representation with the previous STM development, those modifications are not implemented here.

B. Sensor Biases Subset

Sensor biases are reasonably assumed to be stationary band-limited noise processes that are well modeled as exponentially autocorrelated random variables (i.e., first-order Gauss–Markov processes) with a known time constant τ_b. Accordingly, the random process is described by the decaying exponential function

$$\psi(\tau) = \exp(-\Delta t/\tau) \tag{26}$$

which is used to express the appropriate STM for the biases as

$$\boldsymbol{\Phi}_b = \begin{bmatrix} \psi(\tau_b) & 0 \\ 0 & \psi(\tau_b) \end{bmatrix} \tag{27}$$

Note that this process reduces to a white noise sequence for $\tau_b = 0$, or an uncorrelated random walk for $\tau_b \to \infty$. Maneuvering of the servicer spacecraft does not influence the camera biases, and therefore $\boldsymbol{B}_b = 0_{2\times 3}$. Additionally, the biases are additive, and so the associated measurement sensitivity is simply $\boldsymbol{C}_b = \boldsymbol{I}_{2\times 2}$

C. Empirical Accelerations Subset

Just as in the case of the sensor biases, a reasonable model for the evolution of the empirical differential accelerations is provided by considering a first-order Gauss–Markov process similar to the work of Myers and Tapley [35] and Montenbruck et al. [36]. In accordance with this choice, the STM is expressed in terms of the autocorrelation time constant τ_{emp} as

$$\boldsymbol{\Phi}_{\mathrm{emp}} = \begin{bmatrix} \psi(\tau_{\mathrm{emp}}) & 0 & 0 \\ 0 & \psi(\tau_{\mathrm{emp}}) & 0 \\ 0 & 0 & \psi(\tau_{\mathrm{emp}}) \end{bmatrix} \tag{28}$$

Angles-only navigation measurement intervals are typically on the order of tens to several hundreds of seconds, whereas servicer orbital periods can range anywhere from thousands to hundreds of thousands of seconds, depending on the orbit regime. Thus, in order to obtain an appropriate sampling of the characteristic variations in empirical accelerations, the choice of τ_{emp} is inherently orbit dependent as well.

Changes of the servicer orbit due to maneuvering are expected to have a negligible effect on the empirical accelerations, and so $\boldsymbol{B}_{\mathrm{emp}} = 0_{3\times 3}$. Any implications of the empirical accelerations on the evolution of the relative motion (e.g., variations in the ROE) are captured by $\boldsymbol{\Phi}^{\alpha}_{\mathrm{emp}}$, which in turn shows up as expected variations in the modeled measurements through $\boldsymbol{C}_{\alpha}$. Accordingly, $\boldsymbol{C}_{\mathrm{emp}} = 0_{2\times 3}$

Finally, the coupling of $\delta\boldsymbol{a}^{\mathcal{R}}_{\mathrm{emp}}$ and $\delta\boldsymbol{x}_{\alpha}$ is captured by assuming that the empirical accelerations are constant over the propagation time, resulting in an effective Δv vector in the servicer RTN frame expressed as $\delta\boldsymbol{a}^{\mathcal{R}}_{\mathrm{emp}}\Delta t$. The input sensitivity matrix of Eq. (25) then provides

$$\boldsymbol{\Phi}^{\alpha}_{\mathrm{emp}} = \boldsymbol{B}_{\alpha}\Delta t \tag{29}$$

as the final STM component [see Eq. (6)], which allows propagation of the ROE evolution due to $\delta\boldsymbol{a}^{\mathcal{R}}_{\mathrm{emp}}$.

III. Initial Relative Orbit Determination

A proper consideration of the complete filtering procedure must begin with an initialization of the estimated state and state covariance. The presented initial relative orbit determination method makes use of a batch of bearing angle measurements to estimate the initial ROE, with a minimum of three sets (six total data points) needed to reconstruct the six-dimensional state. The two-part algorithm is formulated to operate in arbitrarily eccentric J_2-perturbed orbits. First, an approximate unit vector of the initial ROE state is computed. Then, a solution for the unknown factor that appropriately scales that unit vector is sought using a second-order expansion of the nonlinear measurement model.

A. Solving for the Initial ROE Unit Vector

Recall that Gaias et al. [9] presented results indicating that the observability problem was largely decoupled and that the range ambiguity was well-captured by a single state element $\delta\lambda$. This was

further explored by Sullivan et al. [11], where the IROD approach in that paper used a reduced set of ROEs that were scaled by $\delta\lambda$ to approximately capture the shape and orientation of the relative motion but not the scale. Leveraging the intuition gained from these previous two works, this section is motivated by the fact that a unit vector should exist that accurately describes the shape and direction of the initial ROE, subject only to an unknown scaling factor.

Consider the nonlinear measurement model in Eq. (1). With some algebraic manipulation, it is possible to rearrange this exact model in a linear form with respect to the camera frame relative position, and thus with respect to the RTN frame relative position. The modified measurement model is given as

$$\boldsymbol{H}(\boldsymbol{y}(t))\boldsymbol{R}_{\mathcal{R}}^{\mathcal{C}}\delta\boldsymbol{r}^{\mathcal{R}}(t) = 0_{2\times 1} \tag{30}$$

where

$$\boldsymbol{H}(\boldsymbol{y}(t)) = \begin{bmatrix} c_e & 0 & -s_e \\ 0 & c_\alpha c_e & -s_\alpha \end{bmatrix}$$

Recall that, to the first order, the RTN relative position can be written as

$$\delta\boldsymbol{r}^{\mathcal{R}}(t) = \frac{\partial\delta\boldsymbol{r}^{\mathcal{R}}}{\partial\delta\boldsymbol{x}_{\text{oe}}}\delta\boldsymbol{x}_{\text{oe}}(t) \tag{31}$$

Substituting the preceding equation into Eq. (30) and expressing the ROE state as a function of the initial conditions and the ROE STM yields

$$\hat{\boldsymbol{H}}(t)\boldsymbol{\Phi}_{\text{oe}}(t,t_0)\delta\boldsymbol{x}_{\text{oe}}(t_0) = 0_{2\times 1} \tag{32}$$

where

$$\hat{\boldsymbol{H}}(t) = \boldsymbol{H}(\boldsymbol{y}(t))\boldsymbol{R}_{\mathcal{R}}^{\mathcal{C}}\frac{\partial\delta\boldsymbol{r}^{\mathcal{R}}}{\partial\delta\boldsymbol{x}_{\text{oe}}}$$

With a batch of measurements taken at times t_1 through t_p, successive concatenations of Eq. (32) yields the following condition:

$$\begin{bmatrix} \hat{\boldsymbol{H}}(t_1)\boldsymbol{\Phi}_{\text{oe}}(t_1,t_0) \\ \hat{\boldsymbol{H}}(t_2)\boldsymbol{\Phi}_{\text{oe}}(t_2,t_0) \\ \vdots \\ \hat{\boldsymbol{H}}(t_p)\boldsymbol{\Phi}_{\text{oe}}(t_p,t_0) \end{bmatrix}\delta\boldsymbol{x}_{\text{oe}}(t_0) = \hat{\boldsymbol{\mathcal{O}}}\delta\boldsymbol{x}_{\text{oe}}(t_0) = 0_{2p\times 1} \tag{33}$$

where the modified observability matrix $\hat{\boldsymbol{\mathcal{O}}}$ has been introduced. In the present formulation, it can be shown that this matrix is always full rank but poorly conditioned. Accordingly, $\hat{\boldsymbol{\mathcal{O}}}$ has an empty null space, and the only exact solution to Eq. (33) is the trivial $\delta\boldsymbol{x}_{\text{oe}}(t_0) = 0$. Instead, because $\hat{\boldsymbol{\mathcal{O}}}$ is poorly conditioned (i.e., has a large ratio of maximum to minimum singular values), the approximate nontrivial null space can be determined by considering its singular value decomposition: $\hat{\boldsymbol{\mathcal{O}}} = \boldsymbol{U}\boldsymbol{\Sigma}\boldsymbol{V}^{\mathrm{T}}$. Looking at the modified observability matrix as a linear operator, the columns of $\boldsymbol{V}$ and $\boldsymbol{U}$ describe the input and output directions, respectively, which are scaled by the corresponding singular value entries on the diagonal of $\boldsymbol{\Sigma}$. It follows that the right singular vector associated with the minimum nonzero singular value, $\boldsymbol{v}_1$, approximates the null space of $\hat{\boldsymbol{\mathcal{O}}}$, and thus provides an approximate initial ROE unit vector such that

$$\delta\boldsymbol{x}_{\text{oe}}(t_0) \approx c_1\boldsymbol{v}_1 \tag{34}$$

Here, c_1 is an unknown factor that scales the basis vector to the initial mean ROE state. The complete solution space is spanned by all of the column vectors of $\boldsymbol{V} = [\boldsymbol{v}_1, \boldsymbol{v}_{2:6}]$, such that

$$\delta\boldsymbol{x}_{\text{oe}}(t_0) = c_1\boldsymbol{v}_1 + \boldsymbol{v}_{2:6}\boldsymbol{c}_{2:6} \tag{35}$$

where the remaining scaling factors $\boldsymbol{c}_{2:6}$ are reasonably small compared to c_1. Note that $\boldsymbol{v}_{2:6}\boldsymbol{c}_{2:6}$ denotes the matrix product of the remaining right singular vectors ($\boldsymbol{v}_{2:6} \in \mathbb{R}^{6\times 5}$) with the remaining scaling factors ($c_{2:6} \in \mathbb{R}^5$).

At this stage, a novel closed-form analytical solution has been developed for determining the initial ROE state in eccentric J_2-perturbed orbits, subject only to an unknown set of scaling factors that can justifiably be reduced to a single unknown in accordance with Eq. (34).

B. Analytical Method for Determining the Unknown Scaling Factors

In the aforementioned solution for vector $\boldsymbol{v}_1$, a purely linear transformation is used to map from the ROE to the RTN frame relative position [e.g., Eq. (31)]. In doing so, Eq. (30) can be rewritten as a linear system with respect to the initial ROE in order to arrive at the form of Eq. (35). However, retaining this linear transformation yields a system of homogeneous linear equations where the unknown scalars $[c_1, \boldsymbol{c}_{2:6}]^{\mathrm{T}}$ can be factored out, and thus remain ambiguous. Instead, if the transformation is captured to the second order, Eq. (30) can be rewritten as a system of homogeneous quadratic equations in terms of the unknown scaling factors, and a nontrivial solution can be obtained.

The complete nonlinear transformation from the mean ROE to RTN positions is captured by the function $\boldsymbol{g}(\delta\boldsymbol{x}_{\text{oe}}(t), \text{oe}_s(t))$ in Eq. (24). Expanding this function in a Taylor series about $\delta\boldsymbol{x}_{\text{oe}}(t) = 0$ yields to second order

$$\begin{aligned} \delta r_j^{\mathcal{R}} \approx\ & g_j\Big|_{\substack{0\\ \text{oe}_s}} + \nabla g_j^{\mathrm{T}}\Big|_{\substack{0\\ \text{oe}_s}}\boldsymbol{\Phi}_{\text{oe}}\delta\boldsymbol{x}_{\text{oe}}(t_0) + \ldots \\ & + \frac{1}{2}\delta\boldsymbol{x}_{\text{oe}}(t_0)^{\mathrm{T}}\boldsymbol{\Phi}_{\text{oe}}^{\mathrm{T}}\nabla^2 g_j\Big|_{\substack{0\\ \text{oe}_s}}\boldsymbol{\Phi}_{\text{oe}}\delta\boldsymbol{x}_{\text{oe}}(t_0) \end{aligned} \tag{36}$$

where $\nabla g_j \in \mathbb{R}^6$ and $\nabla^2 g_j \in \mathbb{R}^{6\times 6}$ are the gradient and Hessian of g_j with respect to $\delta\boldsymbol{x}_{\text{oe}}(t)$, respectively, and the STM has been used to rewrite the expansion in terms of the initial ROE state. Substituting Eq. (36) into the modified measurement model [Eq. (30)] and replacing the initial ROE state with the basis expansion in Eq. (35) results in

$$\begin{aligned} 0_{2\times 1} =\ & \boldsymbol{H}\boldsymbol{R}_{\mathcal{R}}^{\mathcal{C}}\boldsymbol{g}\Big|_{\substack{0\\ \text{oe}_s}} + \boldsymbol{H}\boldsymbol{R}_{\mathcal{R}}^{\mathcal{C}}\nabla\boldsymbol{g}\Big|_{\substack{0\\ \text{oe}_s}}\boldsymbol{\Phi}_{\text{oe}}(c_1\boldsymbol{v}_1 + \boldsymbol{v}_{2:6}\boldsymbol{c}_{2:6}) + \ldots \\ & + \frac{1}{2}\boldsymbol{H}\boldsymbol{R}_{\mathcal{R}}^{\mathcal{C}}\begin{pmatrix} (c_1\boldsymbol{v}_1 + \boldsymbol{v}_{2:6}\boldsymbol{c}_{2:6})^{\mathrm{T}}\boldsymbol{\Upsilon}_1(c_1\boldsymbol{v}_1 + \boldsymbol{v}_{2:6}\boldsymbol{c}_{2:6}) \\ (c_1\boldsymbol{v}_1 + \boldsymbol{v}_{2:6}\boldsymbol{c}_{2:6})^{\mathrm{T}}\boldsymbol{\Upsilon}_2(c_1\boldsymbol{v}_1 + \boldsymbol{v}_{2:6}\boldsymbol{c}_{2:6}) \\ (c_1\boldsymbol{v}_1 + \boldsymbol{v}_{2:6}\boldsymbol{c}_{2:6})^{\mathrm{T}}\boldsymbol{\Upsilon}_3(c_1\boldsymbol{v}_1 + \boldsymbol{v}_{2:6}\boldsymbol{c}_{2:6}) \end{pmatrix} \end{aligned} \tag{37}$$

with

$$\boldsymbol{\Upsilon}_j = \boldsymbol{\Phi}_{\text{oe}}(t,t_0)^{\mathrm{T}}\nabla^2 g_j\Big|_{\substack{0\\ \text{oe}_s}}\boldsymbol{\Phi}_{\text{oe}}(t,t_0)$$

For p measurement sets, evaluating Eq. (37) at each measurement time yields $2p$ quadratic equations in terms of the six unknown scaling factors $[c_1, \boldsymbol{c}_{2:6}]^{\mathrm{T}}$. Again, as a bare minimum, three sets of bearing angles are needed. Potential solutions can be posed using nonlinear root-finding techniques such as the Newton–Raphson method, using the nonlinear least squares, or using quadratic optimization. Instead, this paper attempts to make some simplifying assumptions to reduce Eq. (37) to a linear form.

First, the relative RTN frame position components are essentially zero when $\delta\boldsymbol{x}_{\text{oe}} = 0$, and thus $\boldsymbol{g}|_0 \approx 0$. Additionally, the terms containing $\boldsymbol{c}_{2:6}^{\mathrm{T}}(\cdot)\boldsymbol{c}_{2:6}$ can be neglected because they are reasonably smaller than all other terms. Furthermore, if all terms containing $\boldsymbol{c}_{2:6}$ are neglected, the following simplification is achieved:

$$0_{2\times 1} = c_1\boldsymbol{H}\boldsymbol{R}_{\mathcal{R}}^{\mathcal{C}}\nabla\boldsymbol{g}\Big|_{\substack{0\\ \text{oe}_s}}\boldsymbol{\Phi}_{\text{oe}}\boldsymbol{v}_1 + \frac{1}{2}c_1^2\boldsymbol{H}\boldsymbol{R}_{\mathcal{R}}^{\mathcal{C}}\boldsymbol{\Gamma} \tag{38}$$

with

$$\boldsymbol{\Gamma} = \begin{pmatrix} \boldsymbol{v}_1^{\mathrm{T}} \boldsymbol{\Upsilon}_1 \boldsymbol{v}_1 \\ \boldsymbol{v}_1^{\mathrm{T}} \boldsymbol{\Upsilon}_2 \boldsymbol{v}_1 \\ \boldsymbol{v}_1^{\mathrm{T}} \boldsymbol{\Upsilon}_3 \boldsymbol{v}_1 \end{pmatrix}$$

Notice that a power of c_1 can now be factored out. Evaluating the preceding at each measurement time results in $2p$ linear equations in one unknown c_1, which can be solved via linear least squares.

The scaling factor solution using this simplified method displays inconsistent behavior when validating using realistic measurements simulated in high fidelity. This is likely due to neglecting terms that are first order in the dominant scaling factor c_1 in order to achieve a form amenable to linear least squares. Accordingly, the original quadratic equations in Eq. (37) must be reconsidered in future research efforts. A temporary alternative method to obtaining the scaling factor is presented in the following.

C. Obtaining the Scaling Factor from Coarse Prior Information

At this stage, it is necessary to obtain the scaling factor from prior information available to the servicer spacecraft. In general, this information will be a coarse measurement of the relative separation magnitude between the servicer and target, which can be obtained either through the use of NORAD's TLEs or from a designated radar campaign. Conservatively, range errors on the order of at least 10% are expected. The IROD method implemented hereafter solves for the unit vector using the previously established solution and then scales the estimated unit vector by the coarse range measurement provided.

To test the overall functionality of this approach, a Monte Carlo simulation is conducted that assumes that the initial ROE is sampled from a representative multivariate Gaussian distribution and the range measurement is made available to the servicer with an assumed 15% error. The measurements provided to the IROD algorithm are generated using the high-fidelity numerical propagation capability that will be employed in the subsequent filter validation. Table 1 provides the noise parameters assumed for the camera sensor, as well as for the servicer absolute position, velocity, and attitude knowledge. The servicer absolute orbit initial conditions are

$$\begin{aligned} \text{œ}_s(t_0) &= [r_p,\ e,\ i,\ \Omega,\ \omega,\ M_0]^{\mathrm{T}} \\ &= [7200\ \text{km},\ 0.5,\ 30\ \text{deg},\ 60\ \text{deg},\ 120\ \text{deg},\ 180\ \text{deg}]^{\mathrm{T}} \end{aligned} \tag{39}$$

Note that r_p denotes the servicer perigee radius. The multivariate Gaussian mean and standard deviation values for sampling the initial relative state are

$$a_s \delta \bar{\boldsymbol{x}}_{\text{œ}}(t_0) = (-50 \quad -12{,}000 \quad 300 \quad 100 \quad -300 \quad 100)^{\mathrm{T}}\ \text{m} \tag{40}$$

$$a_s \sigma_{\delta \boldsymbol{x}(t_0)} = (25 \quad 5{,}000 \quad 100 \quad 100 \quad 100 \quad 100)^{\mathrm{T}}\ \text{m} \tag{41}$$

Table 1 Sensor noise parameters used in high-fidelity simulation

Parameter	Value
Measurement noise	
$\sigma_{\alpha/\epsilon}$	18 arcsec
$\sigma_{b,\alpha}$	5 arcsec
$\sigma_{b,\epsilon}$	5 arcsec
Servicer knowledge noise	
σ_{pos}	50 m
σ_{vel}	0.50 m/s
$\sigma_{\text{att,off-axis}}$	6 arcsec
$\sigma_{\text{att,roll}}$	40 arcsec

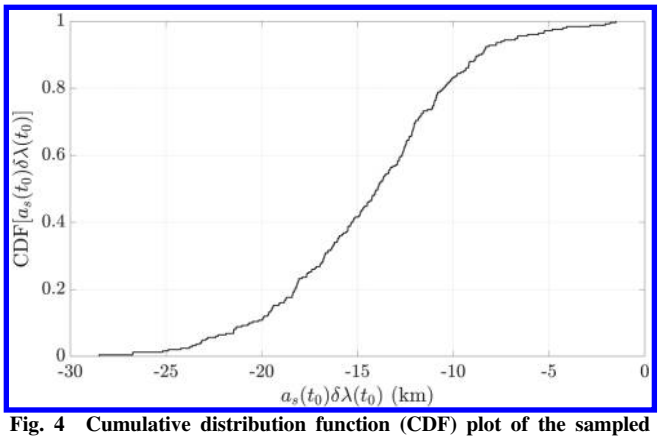

Fig. 4 Cumulative distribution function (CDF) plot of the sampled $a_s(t_0)\delta\lambda(t_0)$ values for the Monte Carlo analysis.

The initial relative orbit geometries are characterized by large mean along-track separations as indicated by large relative mean longitude terms. Accordingly, it is expected that the majority of the range error (in these cases, at the kilometer level) is absorbed by $\delta\lambda$, whereas the remaining five ROEs should be strongly observable and estimated to good accuracy. This is consistent with the intuition that the observability problems are largely confined to the relative mean longitude and that the other parameters accurately describe the shape and orientation of the relative motion. The Monte Carlo simulation consists of 250 runs, wherein the initial ROE is sampled once per run and the number of measurements used in the IROD algorithm is varied from 10 to 60. The cumulative distribution function of $a_s(t_0)\delta\lambda(t_0)$ for the Monte Carlo analysis is shown in Fig. 4 and indicates that the sampling of the relative mean longitude captures a reasonable window of far- to midrange separations in the formation geometry. Measurements are provided at 30 s intervals. The results of this simulation are shown in Table 2 and Figs. A1 and A2 in Appendix A, where the initial ROE estimation error is given as a function of the number of measurement sets used for each of the 250 runs.

As expected, the majority of the scaling factor error is largely absorbed by the $\delta\lambda$ estimate, as seen by constant bands of estimation error in the upper right subplot of Fig. A1. Instead, the remaining five parameters converge to favorable estimates for all simulation runs. Notably, the relative semimajor axis and relative eccentricity components generally converge with a drastic decrease in the sample standard deviation after a large transient error phase of approximately 25 measurements, whereas the relative inclination components are immediately quite accurate, using 10 measurements, and do not improve drastically with more measurements. The Monte Carlo sample mean $\bar{\mu}$ and standard deviation σ statistics when using 10, 30, and 60 measurements are provided in Table 2. Compared with the approach in [11], which required measurements at a sparser interval, the IROD capability tested here represents a distinct improvement because it is generalized to J_2-perturbed orbits of arbitrary eccentricity and requires substantially less measurement time to obtain accurate results. Furthermore, this new method largely confines the initialization error from coarse range information to a single component of the ROE vector $\delta\lambda$. This is a powerful advantage over the methods implemented in the ARGON [2] and AVANTI [3] demonstrations, where the erroneous prior relative position and velocity information from TLEs or radar campaigns is mapped into each element of the ROE state. From a

Table 2 IROD Monte Carlo error statistics

	$a\delta a$, m		$a\delta e_x$, m		$a\delta e_y$, m		$a\delta i_x$, m		$a\delta i_y$, m	
No. of measurements	$\bar{\mu}$	σ	$\bar{\mu}$	σ	$\bar{\mu}$	σ	$\bar{\mu}$	σ	$\bar{\mu}$	σ
10	75.1	97.6	50.2	58.1	61.5	79.2	29.0	7.3	16.2	6.2
30	2.4	3.0	29.2	6.2	6.3	5.6	27.4	7.0	14.7	5.1
60	2.1	2.3	27.9	5.6	6.6	5.3	26.1	7.0	14.0	5.0

space situational awareness perspective, this new method demonstrates the potential to improve initial coarse orbit products by using sparse imaging from a spacecraft in orbit to inform the orbit determination on the strongly observable shape and orientation of the relative orbital motion.

IV. Maneuver-Free Filter Design and Validation

At this stage, the necessary dynamical system framework has been established and the method for filter initialization has been formulated and tested. The following sections highlight the design and validation of an estimation architecture that is better suited to handle the generally weak observability and corresponding numerical sensitivity associated with angles-only navigation. Unlike several previous approaches in angles-only navigation, the algorithms presented here are able to operate without the need for maneuvers dedicated to observability improvement. As a motivation, consider that such a filter architecture effectively decouples the navigation and maneuver-planning processes and enables more fuel-efficient rendezvous by removing the need for frequent observability maneuvers. This design procedure addresses the aforementioned shortcomings in the maneuver-free filter design originally presented by Sullivan et al. [11] for near-circular orbits. The pragmatic improvements are achieved by systematically formulating a filter architecture that is able to make better use of relative motion variations induced by the perturbed dynamical environment while additionally estimating useful parameters that aid in improved convergence speed, consistency, and robustness for relevant orbital geometries.

The EKF is considered as the baseline filter architecture to estimate the ROE state, both for its ubiquity in space navigation applications and to maintain consistency with previous works (see [3,11]). As previously mentioned, the nonlinear dynamics and/or measurement models are accommodated in the EKF by performing a linear Taylor series expansion at each estimation step. Although the EKF allows for direct application of the nonlinear dynamics model in the estimate time-update (or prediction) step, the previously established STM solution is adopted for its ease of implementation and to avoid computationally expensive numerical integration within the filter. As an illustration of the latter advantage, the computational runtimes for multiple state-of-the-art STMs (including the one implemented in this work) were shown in [20] to be several orders of magnitude smaller than numerical integration of high-fidelity nonlinear dynamics. The nonlinear measurement model in Eq. (1) is retained for the measurement-update (or correction) step, and the associated linearization in Eq. (11) is only used to compute the Kalman gain and state covariance update. Instead, the strategic choice to implement the UKF is largely founded in its ability to retain the nonlinear measurement model through all phases of the filtering procedure at practically no extra cost in computational complexity. As previously discussed, accounting for nonlinear model characteristics (particularly those related to osculating effects) improves the filter's ability to map separation-dependent variations in the measured bearing angles to ROE variations that capture range information. The UKF forgoes linearizing the measurement model Taylor series by implementing a stochastic weighted regression procedure. As an improvement to address sensor errors and dynamics modeling deficiencies in the EKF, an augmented-state EKF (AS-EKF) that estimates the sensor biases and empirical differential accelerations is also presented and compared against the baseline architecture. Finally, adaptive forms of the EKF and UKF are formulated to estimate the process noise statistics online in an effort to improve filter stability and performance over a variety of orbit scenarios.

A. Validation Approach

The filter designs are assessed for three nominal relative orbit (RO) scenarios that emulate phases of a rendezvous operation. Servicer absolute orbit initial conditions are given by Eq. (39) and the initial mean ROE test cases describing each of the relative orbit trajectories are provided in Table 3. RO1 is representative of a far-range hold point at initial mean along-track separation of 30 km. RO2 introduces a small difference in the semimajor axis, which enables the servicer to approach the target on a naturally drifting relative trajectory. RO3 describes a leader–follower configuration with a purely along-track separation of 5 km.

Table 3 Relative orbit test cases

	Relative orbital elements, m					
Test case	$a\delta a$	$a\delta\lambda$	$a\delta e_x$	$a\delta e_y$	$a\delta i_x$	$a\delta i_y$
RO1	0	−30,000	500	0	−500	0
RO2	−150	−20,000	300	0	−300	0
RO3	0	−5,000	0	0	0	0

For each test case, the position and velocity of the servicer and target are numerically propagated using rigorous full-force models, including the GRACE Gravity Model 01S (GGM01S) of order and degree 120, a Harris–Priester atmospheric drag model, third-body sun and moon gravity, and solar radiation pressure with a cylindrical Earth shadow model. For an in-depth discussion of this simulation tool, the work by Eddy et al. [37] is recommended. This simulated truth trajectory is then used to generate simulated bearing angles and Global Positioning System (GPS) position/velocity/time solutions that are augmented with additive noise. Recall that Table 1 shows the noise statistics for the bearing angle measurements and biases, as well as the servicer's orbit and attitude knowledge. The bearing angle and attitude noise parameters are consistent with the Blue Canyon Technologies star tracker and attitude determination system [38], and the absolute orbit noise parameters are consistent with GPS weak signal tracking in eccentric orbit [39]. Finally, the numerically propagated position and velocity of the servicer and target are transformed to corresponding osculating orbital element sets (see the work of Schaub and Junkins [29]; Chap. 9) and then numerically averaged to produce the mean elements subject to the above perturbations. Finally, the reference truth ROE are assembled from the numerically computed mean elements according to Eq. (2). All estimation errors are calculated by differencing the output mean ROE of the estimation algorithm from the numerical truth ROE set. To evaluate filter convergence and performance, the estimation error statistics (mean and standard deviation) for each filter test are computed over the last three simulated orbits and tabulated in Tables 4 and 5.

B. Adaptive Noise-Tuning Filter

The selection of Kalman filter process and measurement noise statistics is of interest because it is known that these features can largely influence the filter stability and performance, particularly for nonlinear variants like the EKF and UKF. Process noise is generally included to account for dynamics that are unmodeled by the filter, as well as to aid in stability by keeping the filter receptive to new measurements. As such, a proper selection of process noise statistics could arguably preclude augmenting the estimation state with differential empirical accelerations. The measurement noise statistics are implemented to account for sensor mismodeling in the filter, and they can often be accurately determined by hardware testing. The intent of this section is to develop a mathematical framework for a class of adaptive nonlinear filters that are able to tune the process and/or measurement noise statistics online. This design consideration is founded on the strategy that more accurately accounting for the dynamical processes through an adaptive method can help overcome observability issues related to mismodeling and linearization, and thus mitigate numerical sensitivity and inconsistent filter performances.

Adaptive filtering frameworks have been established in several previous research studies. Most notably, Mehra [40,41] developed the mathematical foundation for four main categories of adaptive filtering methodologies: namely, the Bayesian, maximum likelihood, correlation matching, and covariance matching techniques. Meyers and Tapley [42] further expanded upon the covariance matching technique, and they discussed numerical results in the context of ground-based tracking of LEO satellites. Other research applications for adaptive estimation have been explored in terrestrial target

tracking by Maybeck et al. [43], in spacecraft attitude determination by Mehra et al. [44], and in spacecraft relative navigation using carrier-phase differential GPS by Busse et al. [45]. In the following, an adaptive approach is designed for angles-only relative navigation using the innovation covariance matching technique.

In Kalman filtering, the term *innovation* is generally used to describe the residual formed by the difference between a measurement received by the filter and the expected measurement conditioned on the current state estimate. Alternatively, the term *pre-fit residual* is commonly used in spacecraft orbit determination. This quantity is given by

$$\Delta_k^y = \boldsymbol{y}_k - \boldsymbol{h}(\hat{\boldsymbol{x}}_{k|k-1}) \approx \boldsymbol{y}_k - \boldsymbol{C}_k \hat{\boldsymbol{x}}_{k|k-1} \tag{42}$$

where Δ_k^y denotes the measurement innovation at time step k. Note that $\hat{\boldsymbol{x}}_{i|j}$ denotes the state estimate at time step t_i using measurements up to and including time step t_j. Thus, $\hat{\boldsymbol{x}}_{k|k-1}$ represents the *a priori* (time-updated) state estimate and $\hat{\boldsymbol{x}}_{k|k}$ represents the subsequent *a posteriori* (measurement-updated) estimate at time step t_k. The fundamental idea in innovation covariance matching is to use the statistics of a sample of innovations, in conjunction with their theoretical values, to infer the quantities being adaptively tuned in the filter. To that end, by substituting the linear measurement model given in Eq. (7) for $\boldsymbol{y}_k$ in Eq. (42), the measurement innovation can be rewritten as

$$\Delta_k^y \approx \boldsymbol{C}_k(\boldsymbol{x}_k - \hat{\boldsymbol{x}}_{k|k-1}) + \boldsymbol{\nu}_k \tag{43}$$

The theoretical covariance of Δ_k^y is obtained by applying the expectation operator, resulting in

$$\boldsymbol{\Sigma}_{\Delta_k^y} = \boldsymbol{E}\left[\Delta_k^y \Delta_k^{y^{\mathrm{T}}}\right] = \boldsymbol{C}_k \hat{\boldsymbol{P}}_{k|k-1} \boldsymbol{C}_k^{\mathrm{T}} + \boldsymbol{R}_k \tag{44}$$

On the other hand, if a sample of N innovation sequences is collected in a sliding window, then the sample covariance can be computed as

$$\hat{\boldsymbol{\Sigma}}_{\Delta_k^y} = \frac{1}{N} \sum_{i=k-N+1}^{k} \Delta_i^y \Delta_i^{y^{\mathrm{T}}} \tag{45}$$

Equating Eqs. (44) and (45), and solving for $\boldsymbol{R}_k$, provides an online estimate of the measurement noise covariance matrix. For this paper, it is assumed that the sensors are well modeled and the measurement noise statistics are known accurately enough to not require online estimation. Accordingly, the aforementioned approach will now be extended to estimate the relatively poorly captured process noise statistics.

An analogous state innovation is now defined as the residual formed by the difference between the *a posteriori* state estimate and the *a priori* state estimate:

$$\Delta_k^x = \hat{\boldsymbol{x}}_{k|k} - \hat{\boldsymbol{x}}_{k|k-1} \tag{46}$$

The measurement step of the Kalman filter algorithm provides insight into mapping measurement innovation sequences to state innovation sequences through the Kalman gain $\mathcal{K}_k$. Recall that the state estimate is corrected by scaling the measurement residual (i.e., innovation) using $\mathcal{K}_k$, such that

$$\Delta_k^x = \hat{\boldsymbol{x}}_{k|k} - \hat{\boldsymbol{x}}_{k|k-1} = \mathcal{K}_k(\boldsymbol{y}_k - \boldsymbol{h}(\hat{\boldsymbol{x}}_{k|k-1})) = \mathcal{K}_k \Delta_k^y \tag{47}$$

Accordingly, the process noise covariance can be estimated from a sample of measurement innovations as

$$\boldsymbol{Q}_k = \boldsymbol{E}\left[\Delta_k^x \Delta_k^{x^{\mathrm{T}}}\right] = \mathcal{K}_k \boldsymbol{E}\left[\Delta_k^y \Delta_k^{y^{\mathrm{T}}}\right] \mathcal{K}_k^{\mathrm{T}} = \mathcal{K}_k \boldsymbol{\Sigma}_{\Delta_k^y} \mathcal{K}_k^{\mathrm{T}} \approx \mathcal{K}_k \hat{\boldsymbol{\Sigma}}_{\Delta_k^y} \mathcal{K}_k^{\mathrm{T}} \tag{48}$$

Because the measurement space is generally smaller than the state space (particularly in angles-only navigation), inferring the process noise covariance using samples of measurement innovations (as opposed to other approaches that use state innovations) presents a distinct computational advantage.

As a final note, the estimate of $\boldsymbol{Q}_k$ must abide by the general structure of a covariance matrix. That is, the estimate must be properly adjusted to be symmetric positive semidefinite (SPSD). Accordingly, a procedure inspired by the work of Higham [46] is applied in which the nearest SPSD matrix is obtained through a spectral decomposition of the matrix computed in Eq. (48). In this context, "nearest" indicates that the Frobenius norm of difference between the original and the adjusted covariance matrices is minimized. For further improvement of the numerical stability, a regularization procedure is implemented such that the adjusted process noise covariance matrix estimate does not change substantially over one filtering iteration. This is achieved by placing the following constraint:

$$\max\ \mathrm{eig}(\boldsymbol{Q}_k) \leq \Lambda \cdot \max\ \mathrm{eig}(\boldsymbol{Q}_{k-1}) \tag{49}$$

where the function $\mathrm{eig}(\cdot)$ returns the eigenvalues of the matrix in the argument, and Λ is a regularization factor that controls the allowable relative growth of the covariance estimate based on the maximum eigenvalue.

C. Numerical Results

The filtering strategies are now implemented and validated for estimating the ROE state and the bearing angle biases. The initial ROE estimates and covariances are provided by IROD, and the initial bearing angle biases are initialized to zero with an initial standard deviation of 100 arcsec. Measurements are sparsely received at 300 s intervals, and the measurement noise covariance is assumed to be 18 arcsec. The true bearing angle biases are set to a constant 100 arcsec, and τ_b is chosen as ∞ to model the biases as random walk processes. For the estimation of empirical accelerations in the AS-EKF, τ_{emp} is chosen to be approximately 30 min (10% of the servicer orbital period), which is proportionally consistent with the values chosen by several authors for empirical acceleration estimation in LEO [24,36]. Considering that measurements occur every 5 min and the orbital periods being considered are on the order of several hundred minutes, such a choice for τ_{emp} allows for the acceleration characteristics to be sufficiently sampled using the Gauss–Markov process model. To evaluate filter convergence and performance, the estimation error statistics (mean and standard deviation) for each filter test are computed over the last four simulated orbits and tabulated in Tables 4 and 5. As previously discussed in this paper, and highlighted in other works (see [9,11]), the observability issues are largely confined to estimating the relative mean longitude $a\delta\lambda$. Accordingly, the estimation error and 1-σ filter formal standard deviation of this state element are provided in Appendices B and C (see Figs. B1–B3 and C1a). Note that the estimation error of all other ROE generally scales with the error in the relative mean longitude.

The discussion begins with the RO1 configuration, which does not contain a difference in semimajor axis between the target and servicer. Because the angles-only navigation problem is intrinsically observability constrained when not implementing maneuvers, the relative drift induced by a nonzero semimajor axis difference creates a favorable natural variation in the relative motion that acts similar to a maneuver profile. Additionally, because the magnitudes of the short-period oscillations of the osculating ROE are separation dependent (see Fig. 3), a difference in semimajor axis produces an observable time variation of these magnitudes that is useful for range disambiguation. Accordingly, EKF convergence tends to be more consistent with such geometries, and conversely tends to be less consistent when the orbits are of equal energy (i.e., $a\delta a = 0$). This latter condition is demonstrated in Fig. B1a, where the EKF and adaptive EKF (A-EKF) estimates of $a\delta\lambda$ diverge over the simulation period. The data in Table 4 and the full-state estimation trends in Fig. B4 confirm that the nonzero ROE components ($a\delta e_x$ and $a\delta i_x$) are also estimated poorly (errors on the order of 100 and 60 m, respectively, from the EKF and A-EKF) because their error effectively scales with the relative mean longitude error. Similarly, the AS-EKF estimate of $a\delta\lambda$ diverges, followed by a correspondingly poor estimate of $a\delta e_x$ and $a\delta i_x$. Instead, both the UKF and adaptive UKF (A-UKF) show distinct convergent trends

Table 4 Filter ROE estimation error statistics computed over last four orbits of simulation

		ROE estimation error; $\bar{\mu} \pm \sigma$, m					
Filter	RO	$a\delta a$	$a\delta\lambda$	$a\delta e_x$	$a\delta e_y$	$a\delta i_x$	$a\delta i_y$
EKF	1	2.2 ± 1.5	−6161.0±954.9	104.4 ± 16.5	1.3 ± 1.0	−102.4±16.0	1.1 ± 0.6
	2	−1.8±2.3	130.5 ± 85.1	−7.2±3.5	3.3 ± 1.0	5.1 ± 3.8	−0.2±1.1
	3	0.2 ± 0.2	−2026.0±243.3	−0.1±0.1	0.7 ± 0.1	0.01 ± 0.03	0.01 ± 0.1
AS-EKF	1	1.3 ± 21.6	−2807.0±574.2	113.6 ± 17.7	1.7 ± 15.4	−104.7±25.4	0.2 ± 0.7
	2	9.9 ± 14.5	291.2 ± 87.1	−14.5±13.0	−0.6 ± 10.3	14.7 ± 7.3	1.2 ± 0.7
	3	−0.4±14.9	1329.4 ± 107.2	0.9 ± 7.4	0.4 ± 8.5	0.1 ± 0.4	0.1 ± 0.4
A-EKF	1	0.7 ± 1.0	−3750.0±430.9	61.9 ± 7.0	2.3 ± 0.6	−62.1±7.1	0.4 ± 0.3
	2	2.9 ± 2.4	150.3 ± 113.3	−5.8±4.4	−0.1±0.3	6.0 ± 4.6	0.1 ± 0.3
	3	0.5 ± 0.2	−2319.3±264.9	0.2 ± 0.2	0.4 ± 0.2	0.0 ± 0.1	0.0 ± 0.1
UKF	1	1.6 ± 1.1	566.1 ± 158.5	−8.6±2.7	−1.6±1.0	9.9 ± 2.7	−0.1±0.7
	2	−3.1±2.0	57.1 ± 90.4	−2.5±3.0	2.6 ± 0.8	0.7 ± 3.2	−0.3±1.1
	3	−2.2±0.4	−525.5±84.7	−1.5±0.5	1.7 ± 0.4	0.0 ± 1.0	−0.6±0.9
A-UKF	1	0.1 ± 1.0	147.7 ± 105.8	−4.2±3.5	−0.1 ± 0.7	4.1 ± 3.5	−0.2±0.5
	2	−0.9±0.9	−38.3±48.6	1.4 ± 1.85	0.2 ± 0.3	−1.4±1.9	−0.1±0.2
	3	−0.2±0.3	14.3 ± 29.9	−0.1±0.1	0.3 ± 0.1	0.0 ± 0.1	0.0 ± 0.1

Table 5 Filter bias estimation error statistics computed over last four orbits of simulation

		Bias estimation error; $\bar{\mu} \pm \sigma$, arcsec	
Filter	RO	b_α	b_e
EKF	1	2.84 ± 0.25	19.03 ± 7.01
	2	7.32 ± 0.19	107.36 ± 2.35
	3	3.15 ± 0.27	27.26 ± 2.98
AS-EKF	1	−5.19±0.67	26.13 ± 7.82
	2	−3.35±1.03	17.47 ± 4.38
	3	−2.69±0.51	−32.92±8.50
A-EKF	1	2.64 ± 0.27	10.22 ± 1.30
	2	2.68 ± 0.17	2.07 ± 3.12
	3	3.09 ± 0.23	7.55 ± 4.21
UKF	1	2.93 ± 0.24	−16.88±4.02
	2	7.97 ± 0.21	84.28 ± 0.80
	3	23.35 ± 2.84	32.30 ± 7.11
A-UKF	1	2.31 ± 0.18	−2.62±1.11
	2	2.41 ± 0.19	3.72 ± 1.35
	3	3.60 ± 0.25	9.25 ± 3.35

for the RO1 geometry (see Figs. B1b and B5), with the A-UKF outperforming in both convergence speed and accuracy. Over the last four orbits, the UKF settles to an estimate that is approximately 3% of the true relative mean longitude (error of 566 ± 160) but still maintains accurate estimation of the other ROE parameters within approximately 2%. The A-UKF instead estimates the relative mean longitude to within 148 ± 106 m, which represents a worst-case error that is less than 1% of the true value. Furthermore, the nonzero ROE components are estimated to within 5 m (1%) of their true value, whereas the other components are estimated with submeter-level accuracy. These latter results are a strong indication that the strategic inclusion of a fully nonlinear measurement model in the UKF provides the necessary improvements to overcome the numerical observability constraints ailing the EKF-based filters, whereas the adaptive process noise tuning serves the intended purpose of improving filter performance and convergence speed by supplementing the linear dynamics model within the filter.

With regard to the estimation of azimuth and elevation angle biases in RO1, it is first noteworthy to mention that all filters converge effectively to an accurate estimate of the azimuth bias that is within approximately 3 arcsec of the true value. Recall from Fig. 1 that the azimuth describes the relative motion variation in the cross-track direction, which is not characterized by any mean offsets according to the developed dynamics model. Accordingly, any measurement bias in the azimuth is quickly picked up by the filter. Instead, the elevation angle (which largely captures in-plane relative motion variations) is evidently harder to estimate quickly and accurately. Both Sullivan et al. [11] and D'Amico et al. [2] highlighted an expected bias in the elevation angle that occurred from offsets due to the natural curvature of the orbit. This bias is more pronounced with larger along-track separations. As such, it is generally more difficult for the filter to resolve the overall elevation bias resulting from large along-track separations and intrinsic sensor flaws using a linearized measurement sensitivity model (as in the EKF) that does not fully account for the curvature effect. Although the EKF, A-EKF, and A-UKF estimate the elevation bias to within approximately 20 arcsec over the last four simulated orbits, only the A-UKF is able to effectively achieve estimation accuracy that is comparable to the azimuth bias results (approximately 4 arcsec). The estimation error trends and 1-σ bounds of the elevation bias are shown in Fig. B6 for RO1.

The ROE estimation results for RO2 are shown in Fig. B2 for the (A-)EKF and (A-)UKF, and they are shown in Fig. C1 for the AS-EKF. The illustrated trends largely confirm the conclusion from Sullivan et al. [11] that a difference in semimajor axes produces a sufficient amount of long-term variation in the relative motion and short-period oscillation magnitudes to achieve reasonable filter convergence. This is evidenced by the ability of the EKF and A-EKF (see Fig. B2a) to estimate $a\delta\lambda$ to within 130 ± 85 and 150 ± 113 m, respectively, over the last four simulated orbits. Note from the figures that the inclusion of adaptive process noise tuning effectively decreases the necessary time to convergence by approximately four orbits. The AS-EKF achieves an estimation error of 291 ± 87 m, which is far better than the performance achieved by that filter in other RO configurations (see Table 4 and Fig. C1a), and it demonstrates quicker convergence than the standard EKF counterpart. As compared with the EKF-based approaches, the UKF-based results show even better convergence accuracy, with the UKF estimating the relative mean longitude to within 57 ± 90 m and the A-UKF estimating to within 38 ± 49 m. Note that the adaptive process noise tuning for the A-UKF improves both filter convergence speed (see Fig. B2b) and steady-state standard deviation of the estimate. As expected, all filters achieve good estimation accuracy of the azimuth bias, with the adaptive filters outperforming their standard counterparts by approximately 5 arcsec. For the elevation bias, Figs. B7a and B7b indicate that the EKF and UKF struggle to arrive at accurate estimates (errors of 107 ± 2 and 84 ± 1 arcsec, respectively). Instead, the AS-EKF shows substantial improvement, achieving an elevation bias error of 17.5 ± 4 arcsec. As before, the adaptive filters instead enable the elevation bias to be captured more effectively, with errors of 2 ± 3 and 4 ± 1 arcsec for the A-EKF and A-UKF, respectively. The insight here is that the filter is able to pick up the bearing angle biases more effectively because the process noise model is being adaptively improved, which leads to a better correlation between the observed bearing angle trends and the propagated ROE within the filter.

A depiction of the estimated differential empirical accelerations obtained by the AS-EKF for RO2 is shown in Fig. C2 and compared

with the true differential accelerations from the numerical propagation. These results indicate that the filter is able to reasonably capture the order of magnitude ($\approx 10^{-5}$ ms^{-2}) and periodicity of the perturbation effects that are not considered in the filter dynamics model. Note that, for the orbit scenarios considered in this paper, the dominant unmodeled perturbations are the J_3 zonal harmonic and atmospheric drag.

Finally, the estimation of the RO3 geometry is simulated and the ROE error trends are provided in Fig. B3, followed by the elevation bias trends in Fig. B8. Note that this geometry is marked by only pure along-track separation, where the target appears very nearly constant in the image frame. The only variations in the relative motion that the filter can rely upon to reconstruct the range are due to the differential perturbation effects, which cause slight oscillations in the bearing angles on the order of a few hundred arcseconds. Accordingly, without a highly accurate measurement model, the observability issues are irreconcilable and the estimate is likely to diverge. This behavior is evident in the performance of the EKF and A-EKF (see Fig. B3a), as well as the AS-EKF, where the relative mean longitude estimate diverges over time. Even though $a\delta\lambda$ is diverging, Table 4 shows that the filters are able to estimate all other components of the ROE vector to high accuracy. This is again largely because the unobservability is confined to the relative mean longitude; thus, the filter is able to definitively determine the shape of the relative motion (i.e., all nonzero ROE errors should scale with the relative mean longitude knowledge). Once again, where the EKF-based approaches fail to converge to stable and accurate estimates, the UKF-based approaches succeed (see Fig. B3b). In the RO3 case, the UKF displays a clear yet slow convergent phase. Over the last four orbits, it achieves an estimation error of 525 ± 85 m, which is still substantial but markedly improved over the EKF and A-EKF results. Instead, the A-UKF estimates $a\delta\lambda$ to within 14 ± 30 m, which represents a worst-case error that is just under 1% of the true value. As in the previous cases, the adaptive filters are better able to estimate the elevation bias with good accuracy as compared to the standard filter variants. The A-EKF and A-UKF, respectively, achieve errors of 8 ± 4 arcsec and 9 ± 3 arcsec, which offer a substantial improvement over the EKF and UKF errors on the order of 30 arcsec.

Overall, there are several definitive and critical trends in the estimation results presented here. First, in the cases where the bearing angles are only varying due to subtle oscillations imposed by the differential osculating perturbation effects in orbits of equal energy (i.e., $\delta a = 0$), the EKF-based approaches simply fail. It stands to reason that the necessary linearization of the measurement model effectively precludes a proper mapping of observed bearing angle trends to a correspondingly accurate estimate of the relative motion trends that properly rectifies the relative separation. This fact is seen clearly in the full-state estimation errors and 1-σ bounds for the RO1 configuration shown in Fig. B4. Instead, the UKF-based approaches display distinct stability and convergence phases in all relative motion configurations. See Fig. B5 for an example of the full ROE state estimation errors and 1-σ bounds for the RO1 configuration. These results illustrate the importance of retaining nonlinearities (particularly those separation-dependent effects related to the orbit curvature and oscillatory perturbed motion) in the measurement model. Furthermore, the inclusion of adaptive process noise tuning has definitively served the purpose of improving convergence accuracy and speed for all instances where the standard counterpart is already stable but slower to converge. Although the A-EKF models in RO1 and RO3 still show divergence, it is evident that the process noise tuning is attempting to correct for this but cannot overcome the limitations imposed by the measurement model linearization. Finally, the A-UKF outperforms all other filtering strategies when considering the ROE estimation accuracy, speed, stability (as evidenced by error standard deviation), and robustness (as evidenced by consistent estimation in all geometries), as well as the effective estimation of the sensor bearing angle biases. This estimator consistently delivers estimation errors of the relative mean longitude (and thus the range) that are within 1% of the true value while also estimating the remaining ROE at meter and submeter levels throughout.

V. Conclusions

This research has addressed the problem of developing filter algorithms that do not require maneuvering to estimate the relative orbital motion of a target space object with respect to an observing spacecraft using only bearing angles received by the servicer onboard camera. As part of the estimation architecture development, the problem of angles-only initial relative orbit determination was addressed to provide an initialization to the sequential navigation filter. Unlike other approaches that constrain the initial relative orbit determination problem to circular unperturbed orbits, the method in this paper was formulated for implementation in eccentric J_2-perturbed orbits. Although the approach was shown to accurately capture the unit vector associated with the initial relative orbital element state, the solution for the necessary scaling factor to complete the unique initialization suffered from the simplifying assumptions used to attempt a linear least-squares solution. Still, the definitive advantages of the new solution procedure were evidenced by the consistent initialization accuracy for a multitude of relative motion geometries while requiring less total measurement time and only relying on coarse range knowledge with kilometer-level error.

With regard to the sequential estimation architectures developed in this work, several key lessons were learned. First, in assessing the ability of the extended Kalman filter to estimate the relative orbital element state, inconsistent performances for several relative motion scenarios provided a strong indication that the dynamics and measurement model linearizations required by the extended KF (EKF) substantially limited the achievable observability and, accordingly, the filter consistency and accuracy. From there, augmenting the estimation state to include empirical accelerations and sensor biases that supplement the truncated process and measurement models in the EKF yielded incremental improvements in the filter performance for relative motion cases that plagued the original design implementation. Although the augmented-state EKF still demonstrated distinct inconsistency and slow convergence in estimating the relative orbital element (ROE) and sensor biases for the majority of simulated orbital geometries, the improved filter convergence speed for relative orbit geometries with a difference in semimajor axes suggested that an alternative method to supplement the filter process model could improve the overall estimation capability. Accordingly, an adaptive variant of the EKF that tuned the process noise statistics online was developed and validated. The adaptive EKF did not show substantial improvement over the augmented-state EKF. Instead, by leveraging the ability to forgo measurement model linearization while retaining the simplicity of linear dynamics in the unscented Kalman filter framework, the filter performance showed distinct stability and performance advantages in cases where there was not a large variation of the relative motion due to a nonzero difference in the semimajor axis. This was largely due to the unscented KF (UKF) ability to accurately correlate nonlinear separation-dependent osculating and orbit curvature effects observed in the bearing angle measurements to improved separation-rectified variations in the relative motion. This deeper systematic inclusion of perturbed relative motion effects in the measurement model was entirely enabled by the use of mean relative orbital elements as the filter state parameterization. With the filter stability issues resolved, the design process moved toward improving convergence speed and accuracy. Thus, the strategic choice was made to supplement the linearized dynamics model with adaptive process noise tuning. This adaptive UKF outperformed every other variant across the board (including in the particularly difficult pure along-track separation case), estimating the ROE state and sensor biases to higher accuracy with faster convergence than previous designs and with formal covariances that accurately reflected the true error trends. The results conclusively demonstrated that a systematic method for capturing the nonlinear effects of orbit curvature and dominant perturbations in a filter measurement model, combined with supplementation of an efficient linear dynamics model by adaptive process noise tuning, enabled improved maneuver-free angles-only navigation in eccentric orbits.

Appendix A: Numerical Results: Initial Relative Orbit Determination

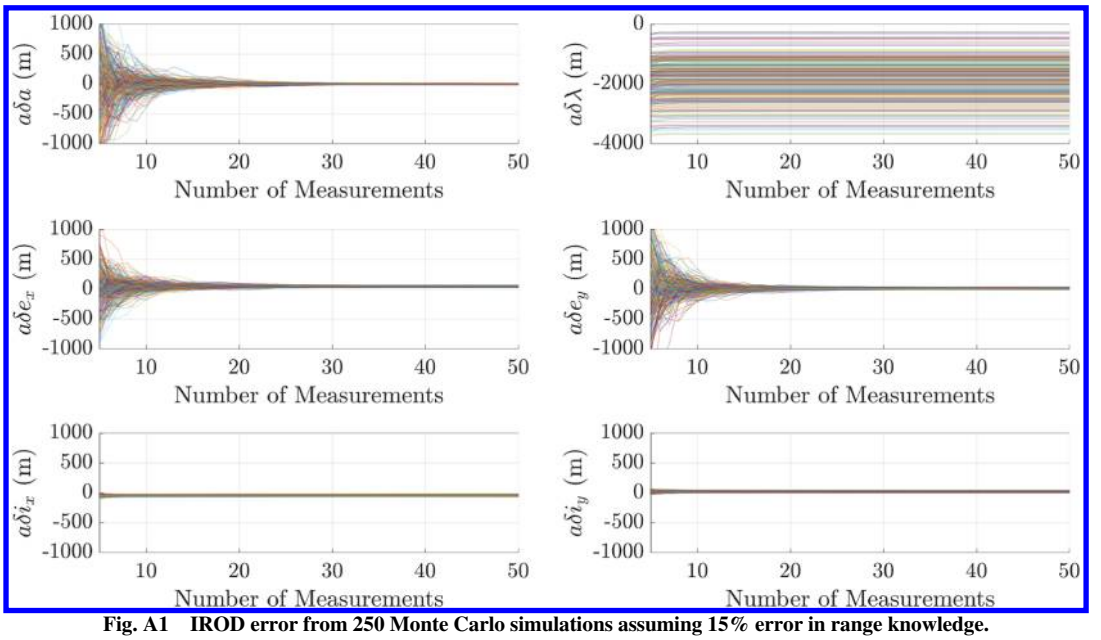

Fig. A1 IROD error from 250 Monte Carlo simulations assuming 15% error in range knowledge.

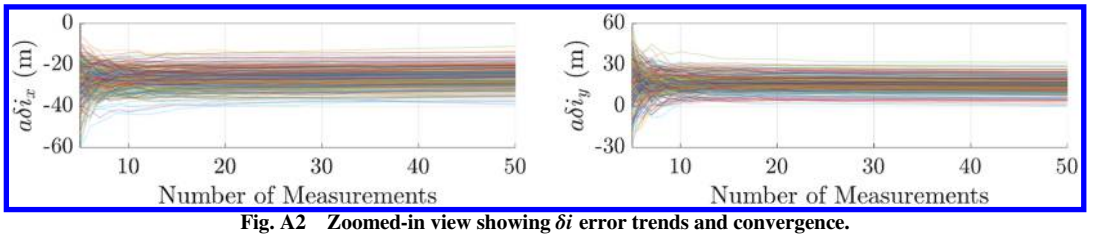

Fig. A2 Zoomed-in view showing δi error trends and convergence.

Appendix B: Numerical Results: Standard and Adaptive Filters

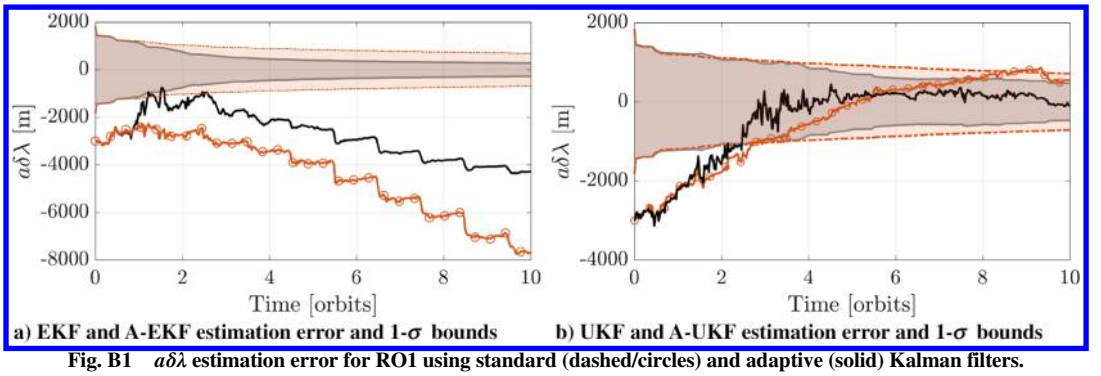

Fig. B1 $a\delta\lambda$ estimation error for RO1 using standard (dashed/circles) and adaptive (solid) Kalman filters.

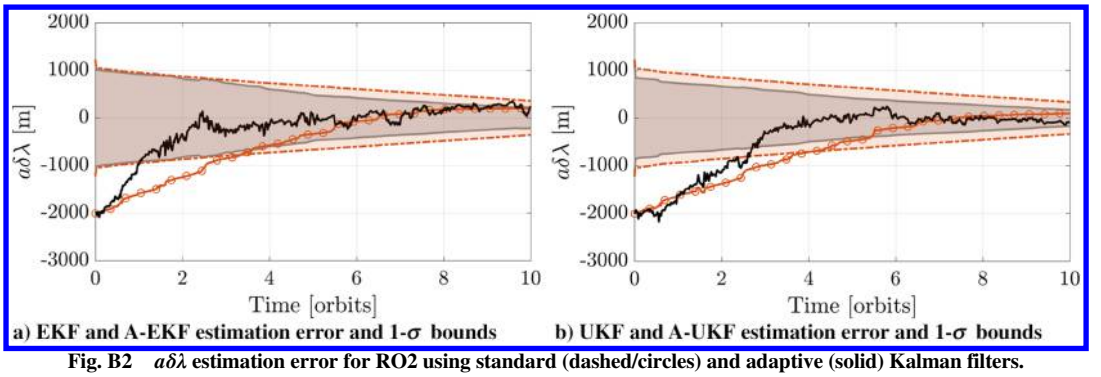

Fig. B2 $a\delta\lambda$ estimation error for RO2 using standard (dashed/circles) and adaptive (solid) Kalman filters.

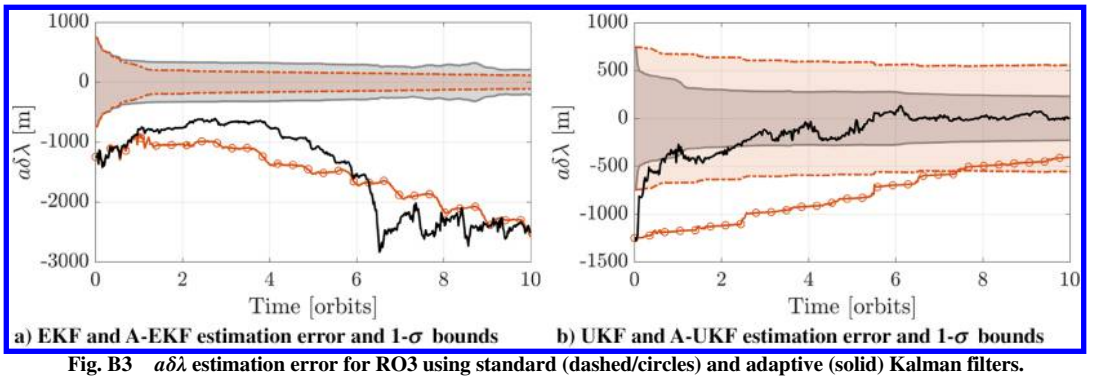

Fig. B3 $a\delta\lambda$ **estimation error for RO3 using standard (dashed/circles) and adaptive (solid) Kalman filters.**

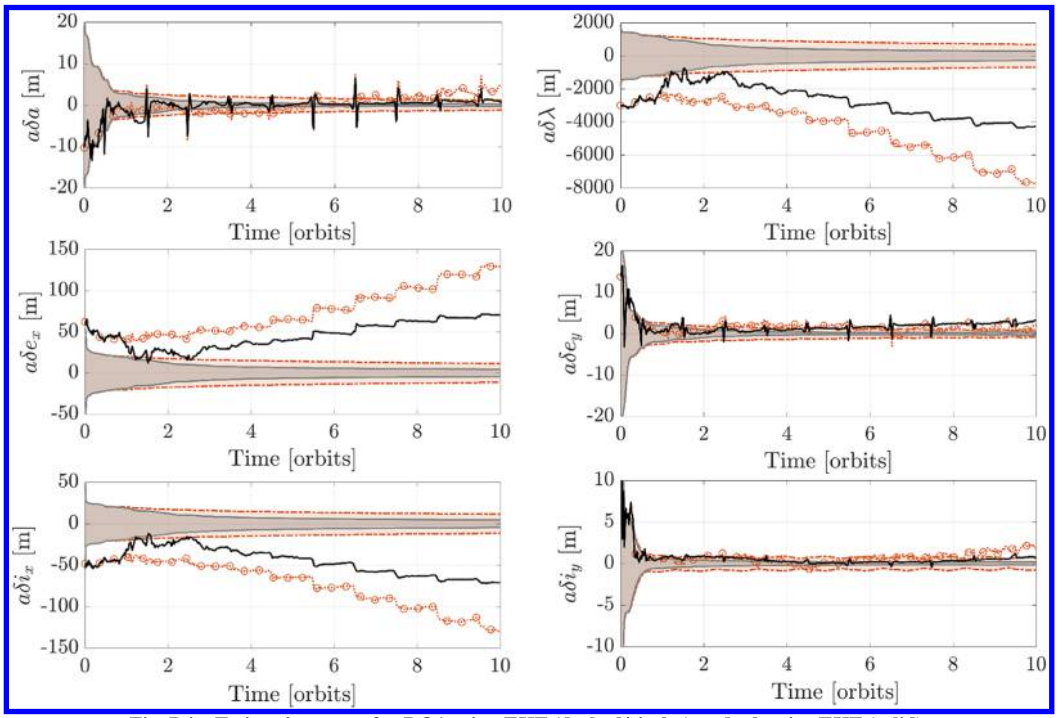

Fig. B4 Estimation error for RO1 using EKF (dashed/circles) and adaptive EKF (solid).

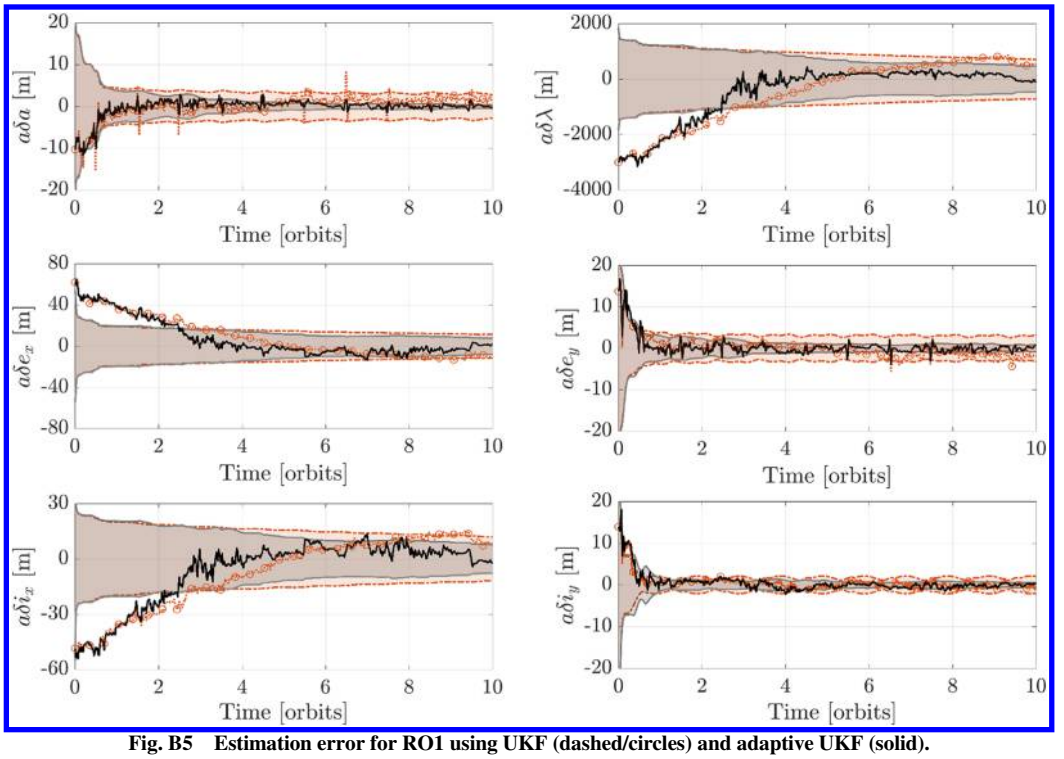

Fig. B5 Estimation error for RO1 using UKF (dashed/circles) and adaptive UKF (solid).

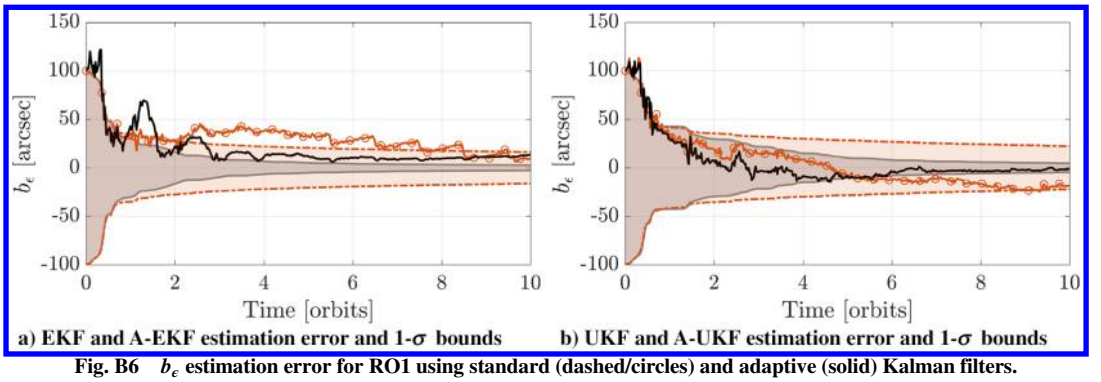

Fig. B6 b_ϵ estimation error for RO1 using standard (dashed/circles) and adaptive (solid) Kalman filters.

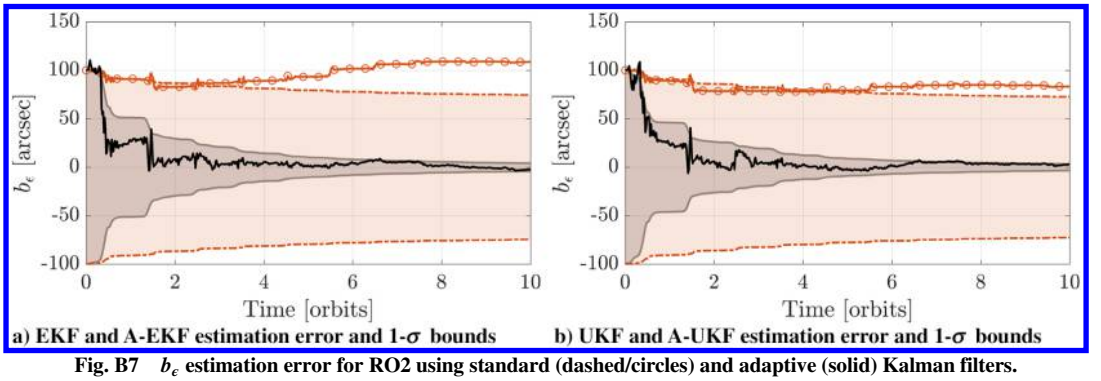

Fig. B7 b_ϵ estimation error for RO2 using standard (dashed/circles) and adaptive (solid) Kalman filters.

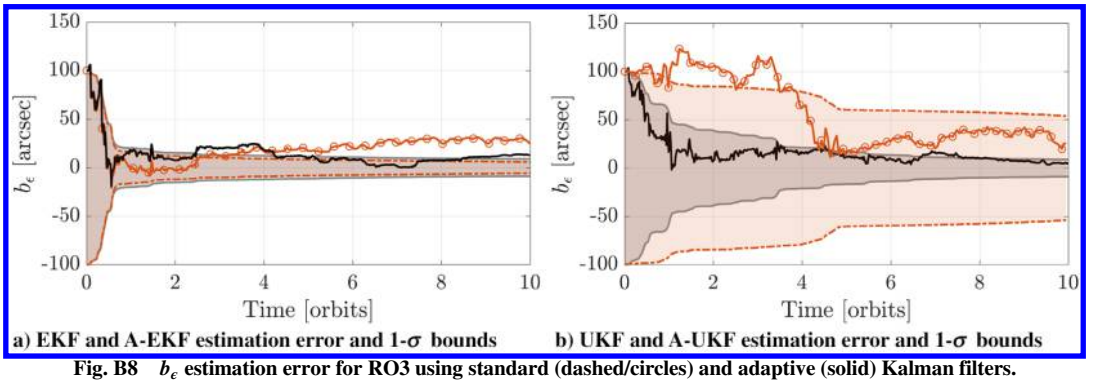

Fig. B8 b_ϵ estimation error for RO3 using standard (dashed/circles) and adaptive (solid) Kalman filters.

Appendix C: Numerical Results: Augmented-State Extended Kalman Filter for RO2 Test

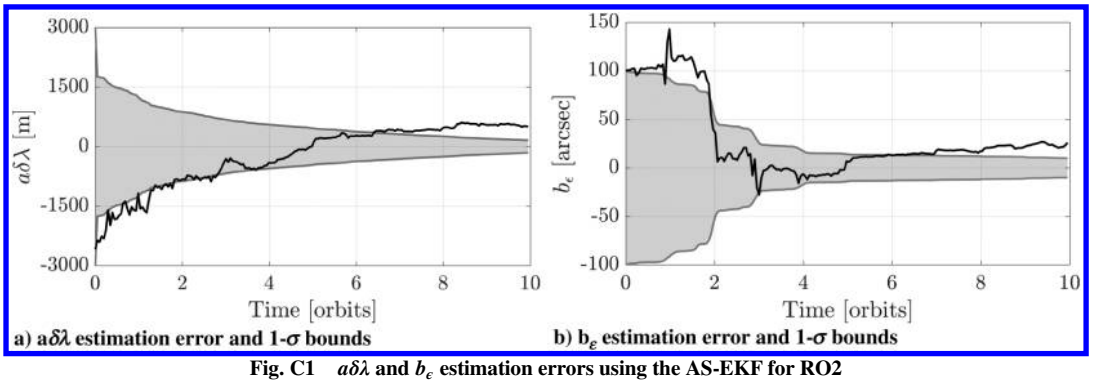

Fig. C1 $a\delta\lambda$ and b_ϵ estimation errors using the AS-EKF for RO2

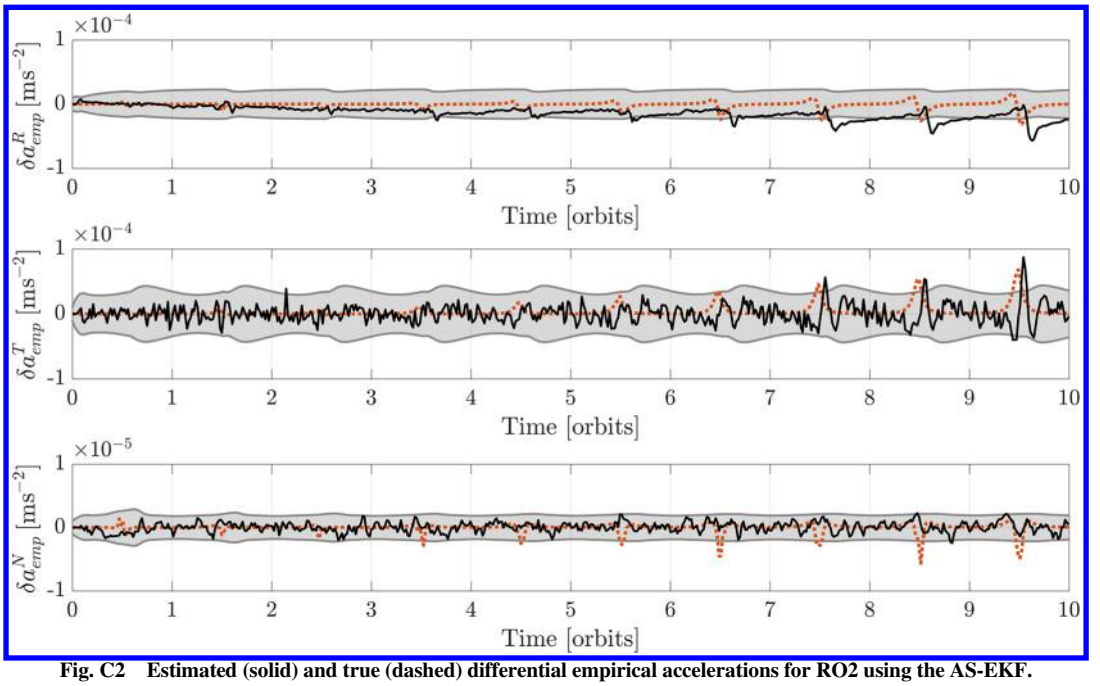

Fig. C2 Estimated (solid) and true (dashed) differential empirical accelerations for RO2 using the AS-EKF.

Acknowledgments

This work was supported by the U.S. Air Force Research Laboratory's Control, Navigation, and Guidance for Autonomous Spacecraft contract FA9453-16-C-0029. The authors are thankful for their support.

References

[1] D'Amico, S., Pavone, M., Saraf, S., Alhussien, A., Al-Saud, T., Buchman, S., Bryer, R., and Farhat, C., "Miniaturized Autonomous Distributed Space Systems for Future Science and Exploration," *8th International Workshop of Spacecraft Formation Flying*, Delft Univ., Delft, The Netherlands, 2015.

[2] D'Amico, S., Ardaens, J.-S., Gaias, G., Benninghoff, H., Schlepp, B., and Jrgensen, J. L., "Noncooperative Rendezvous Using Angles-Only Optical Navigation: System Design and Flight Results," *Journal of Guidance, Control, and Dynamics*, Vol. 36, No. 6, 2013, pp. 1576–1595. doi:10.2514/1.59236

[3] Gaias, G., Ardaens, J.-S., and D'Amico, S., "The Autonomous Vision Approach Navigation and Target Identification (AVANTI) Experiment: Objectives and Design," *9th International ESA Conference on Guidance, Navigation and Control Systems*, Porto, Portugal, 2014.

[4] Kolmas, J., Banazadeh, P., Koenig, A. W., D'Amico, S., and Macintosh, B., "System Design of a Miniaturized Distributed Occulter/Telescope for Direct Imaging of Star Vicinity," *2016 IEEE Aerospace Conference*, IEEE, Piscataway, NJ, 2016, pp. 1–11.

[5] D'Amico, S., and Spurmann, J., "Formation Flying Concept for DEOS," DLR, German Aerospace Center TR DLR- GSOC TN 10-07, Weissling, Germany, 2010.

[6] Sellmaier, F., Boge, T., Spurmann, J., Gully, S., Rupp, T., and Huber, F., "On-Orbit Servicing Missions: Challenges and Solutions for Spacecraft Operations," AIAA Paper 2010-2159, April 2010. doi:10.2514/6.2010-2159

[7] Reed, B. B., Smith, R. C., Naasz, B. J., Pellegrino, J. F., and Bacon, C. E., "The Restore-L Servicing Mission," *AIAA SPACE 2016*, AIAA Paper 2016-5478, 2016, pp. 5478–5485. doi:10.2514/6.2016-5478

[8] Woffinden, D. C., and Geller, D. K., "Observability Criteria for Angles-Only Navigation," *IEEE Transactions on Aerospace and Electronic Systems*, Vol. 45, No. 3, 2009, pp. 1194–1208. doi:10.1109/TAES.2009.5259193

[9] Gaias, G., D'Amico, S., and Ardaens, J.-S., "Angles-Only Navigation to a Noncooperative Satellite Using Relative Orbital Elements," *Journal of Guidance, Control, and Dynamics*, Vol. 37, No. 2, 2014, pp. 439–451. doi:10.2514/1.61494

[10] Woffinden, D. C., and Geller, D. K., "Optimal Orbital Rendezvous Maneuvering for Angles-Only Navigation," *Journal of Guidance, Control, and Dynamics*, Vol. 32, No. 4, 2009, pp. 1382–1387. doi:10.2514/1.45006

[11] Sullivan, J., Koenig, A., and D'Amico, S., "Improved Maneuver-Free Approach to Angles-Only Navigation for Space Rendezvous," *26th AAS/AIAA Space Flight Mechanics Conference*, AAS Paper 16-530, Napa, CA, 2016.

[12] D'Amico, S., and Montenbruck, O., "Proximity Operations of Formation-Flying Spacecraft Using an Eccentricity/Inclination Vector Separation," *Journal of Guidance, Control, and Dynamics*, Vol. 29, No. 3, 2006, pp. 554–563. doi:10.2514/1.15114

[13] Geller, D., and Lovell, T. A., "Non-Iterative Approximate Solution to the Angles-Only Initial Relative Orbit Determination Problem in Spherical Coordinates," *AIAA/AAS Space Flight Mechanics Conference*, AAS Paper 16-356, Napa, CA, 2016.

[14] Newman, B., Lovell, T. A., Pratt, E., and Duncan, E., "Hybrid Linear-Nonlinear Initial Orbit Determination with Single Iteration Refinement for Relative Motion," *Advances in the Astronautical Sciences*, Vol. 155, Univelt, Escondido, CA, 2015, pp. 2149–2168.

[15] Kalman, R. E., "A New Approach to Linear Filtering and Prediction Problems," *Journal of Basic Engineering*, Vol. 82, No. 1, 1960, pp. 35–45. doi:10.1115/1.3662552

[16] Kalman, R. E., and Bucy, R. S., "New Results in Linear Filtering and Prediction Theory," *Journal of Basic Engineering*, Vol. 83, No. 1, 1961, pp. 95–108. doi:10.1115/1.3658902

[17] Kalman, R. E., "New Methods in Wiener Filtering Theory," *Proceedings of the 1st Symposium on Engineering Applications of Random Function Theory and Probability*, 1963.

[18] Bucy, R. S., "Linear and Nonlinear Filtering," *Proceedings of the IEEE*, Vol. 58, No. 6, 1970, pp. 854–864. doi:10.1109/PROC.1970.7792

[19] Julier, S. J., and Uhlmann, J. K., "New Extension of the Kalman Filter to Nonlinear Systems," *International Society for Optics and Photonics Conference*, 1997, pp. 182–193.

[20] Sullivan, J., Grimberg, S., and D'Amico, S., "Comprehensive Survey and Assessment of Spacecraft Relative Motion Dynamics Models," *Journal of Guidance, Control, and Dynamics*, April 2017. doi:10.2514/1.G002309

[21] Koenig, A. W., Guffanti, T., and D'Amico, S., "New State Transition Matrices for Relative Motion of Spacecraft Formations in Perturbed Orbits," *Journal of Guidance, Control, and Dynamics*, Vol. 40, No. 7, July 2017, pp. 1749–1768. doi:10.2514/1.G002409

[22] Spiridonova, S., "Formation Dynamics in Geostationary Ring," *Celestial Mechanics and Dynamical Astronomy*, Vol. 125, No. 4, 2016, pp. 485–500. doi:10.1007/s10569-016-9693-0

[23] Guffanti, T., D'Amico, S., and Lavagna, M., "Long-Term Analytical Propagation of Satellite Relative Motion in Perturbed Orbits," *27th AAS/AIAA Space Flight Mechanics Meeting*, AAS Paper 17-355, San Antonio, TX, Feb. 2017.

[24] D'Amico, S., "Autonomous Formation Flying in Low Earth Orbit," Ph. D. Thesis, Delft Univ., Delft, The Netherlands, 2010.

[25] Casotto, S., "Position and Velocity Perturbations in the Orbital Frame in Terms of Classical Element Perturbations," *Celestial Mechanics and Dynamical Astronomy*, Vol. 55, No. 3, 1993, pp. 209–221. doi:10.1007/BF00692510

[26] Schaub, H., "Relative Orbit Geometry Through Classical Orbit Element Differences," *Journal of Guidance, Control, and Dynamics*, Vol. 27, No. 5, 2004, pp. 839–848. doi:10.2514/1.12595

[27] Alfriend, K., Vadali, S. R., Gurfil, P., How, J., and Breger, L., *Spacecraft Formation Flying: Dynamics, Control and Navigation*, Vol. 2, Butterworth-Heinemann, London, 2009.

[28] Yamanaka, K., and Ankersen, F., "New State Transition Matrix for Relative Motion on an Arbitrary Elliptical Orbit," *Journal of Guidance, Control, and Dynamics*, Vol. 25, No. 1, 2002, pp. 60–66. doi:10.2514/2.4875

[29] Schaub, H., and Junkins, J. L., *Analytical Mechanics of Space Systems*, AIAA Education Series, AIAA, Reston, VA, 2003.

[30] Gim, D.-W., and Alfriend, K. T., "State Transition Matrix of Relative Motion for the Perturbed Noncircular Reference Orbit," *Journal of Guidance, Control, and Dynamics*, Vol. 26, No. 6, 2003, pp. 956–971. doi:10.2514/2.6924

[31] Gim, D.-W., and Alfriend, K. T., "Satellite Relative Motion Using Differential Equinoctial Elements," *Celestial Mechanics and Dynamical Astronomy*, Vol. 92, No. 4, 2005, pp. 295–336. doi:10.1007/s10569-004-1799-0

[32] D'Amico, S., "Relative Orbital Elements as Integration Constants of Hill's Equations," DLR, German Aerospace Center TR DLR-GSOC TN 05-08, Weissling, Germany, 2005.

[33] Riggi, L., and D'Amico, S., "Optimal Impulsive Closed-Form Control for Spacecraft Formation Flying and Rendezvous," *American Control Conference*, Boston, MA, 2016, pp. 5854–5861.

[34] Chernick, M., and D'Amico, S., "New Closed-Form Solutions for Optimal Impulsive Control of Spacecraft Relative Motion," *AIAA Space and Astronautics Form and Exposition*, AIAA Paper 2016-5659, 2016.

[35] Myers, K., and Tapley, B., "Dynamical Model Compensation for Near-Earth Satellite Orbit Determination," *Journal of Guidance, Control, and Dynamics*, Vol. 13, No. 3, 1975, pp. 343–349. doi:10.2514/3.49702

[36] Montenbruck, O., Helleputte, T. V., Kroes, R., and Gill, E., "Reduced Dynamic Orbit Determination Using GPS Code and Carrier Measurements," *Journal of Aerospace Science and Technology*, Vol. 9, No. 3, 2005, pp. 261–271. doi:10.1016/j.ast.2005.01.003

[37] Eddy, D., Giralo, V., and D'Amico, S., "Development and Verification of the Stanford GNSS Navigation Testbed for Spacecraft Formation-Flying," Space Rendezvous Lab. SLAB TN 17-06, Stanford, CA, 2017.

[38] Palo, S., Stafford, G., and Hoskins, A., "An Agile Multi-Use Nano Star Camera for Constellation Applications," *27th Annual AIAA/USU Conference on Small Satellites*, Paper SSC13-III-5, Logan, UT, 2013.

[39] Farahmand, M., Long, A., and Carpenter, R., "Magnetospheric Multiscale Mission Navigation Performance Using the Goddard Enhanced Onboard Navigation System," *Proceedings of the 25th International Symposium on Space Flight Dynamics*, 2015.

[40] Mehra, R., "Approaches to Adaptive Filtering," *IEEE Transactions on Automatic Control*, Vol. 17, No. 5, Oct. 1972, pp. 693–698.

[41] Mehra, R., "On the Identification of Variances and Adaptive Kalman Filtering," *IEEE Transactions on Automatic Control*, Vol. 15, No. 2, 1970, pp. 175–184. doi:10.1109/TAC.1970.1099422

[42] Myers, K., and Tapley, B., "Adaptive Sequential Estimation with Unknown Noise Statistics," *IEEE Transactions on Automatic Control*, Vol. 21, No. 4, 1976, pp. 520–523. doi:10.1109/TAC.1976.1101260

[43] Maybeck, P. S., Jensen, R. L., and Harnly, D. A., "An Adaptive Extended Kalman Filter for Target Image Tracking," *IEEE Transactions on Aerospace and Electronic Systems*, Vol. AES-17, No. 2, 1981, pp. 173–180. doi:10.1109/TAES.1981.309143

[44] Mehra, R., Seereeram, S., Bayard, D., and Hadaegh, F., "Adaptive Kalman Filtering, Failure Detection and Identification for Spacecraft Attitude Estimation," *Proceedings of the 4th IEEE Conference on Control Applications 1995*, IEEE, Piscataway, NJ, 1995, pp. 176–181.

[45] Busse, F. D., How, J. P., and Simpson, J., "Demonstration of Adaptive Extended Kalman Filter for Low-Earth-Orbit Formation Estimation Using CDGPS," *Navigation*, Vol. 50, No. 2, 2003, pp. 79–93. doi:10.1002/navi.2003.50.issue-2

[46] Higham, N. J., "Computing a Nearest Symmetric Positive Semidefinite Matrix," *Linear Algebra and Its Applications*, Vol. 103, May 1988, pp. 103–118. doi:10.1016/0024-3795(88)90223-6